# Radiative sensitivity quantified by a new set of radiation flux kernels based on the ERA5 reanalysis

Han Huang, Yi Huang

Department of Atmospheric and Oceanic Sciences, McGill University, Montreal, Canada

Corresponding Authors:

Han Huang, han.huang2@mcgill.ca (ORCID: 0000-0002-9143-6453),

Yi Huang, yi.huang@mcgill.ca (ORCID: 0000-0002-5065-4198)

# Abstract

Radiative sensitivity, i.e., the response of the radiative flux to climate perturbations, is essential to understanding climate variability. The sensitivity kernels computed by radiative transfer models have been broadly used for assessing the climate forcing and feedbacks for global warming. As these assessments are largely focused on the top of atmosphere (TOA) radiation budget, less attention has been paid to the surface radiation budget or the associated surface radiative sensitivity kernels. Based on the fifth generation European Center for Medium-Range Weather Forecasts (ERA5) atmospheric reanalysis, we produce a new set of radiative kernels for both the TOA and surface radiative fluxes, which is made available at http://dx.doi.org/10.17632/vmg3s67568.2 (Huang and Huang, 2023). By comparing with other published radiative kernels, we find that the TOA kernels are generally in agreement in terms of global mean radiative sensitivity and analyzed overall feedback strength. The unexplained residual in the radiation closure tests is found to be generally within 10%, no matter which kernel dataset is used. The uncertainty in the TOA feedbacks caused by inter-kernel differences, as measured by the standard deviation of the global mean feedback parameter value is much smaller than the inter-climate model spread of the feedback values. However, we find relatively larger discrepancies in the surface kernels. The newly generated ERA5 kernel outperforms many other datasets in closing the surface energy budget, achieving a radiation closure comparable to the TOA feedback decomposition, which affirms the validity of kernel method for the surface radiation budget analysis. In this paper, we provide a detailed description on how ERA5 kernels are generated and considerations to ensure proper use of them in feedback quantifications.

## 1. Introduction

Radiative kernels measure the sensitivity of radiative fluxes to the perturbation of feedback variables, such as temperature, water vapor, albedo and cloud (e.g., Soden and Held, 2006; Huang et al., 2007; Shell et al., 2008; Previdi, 2010; Zelinka et al., 2012; Block and Mauritsen, 2013; Yue et al., 2016; Huang et al., 2017; Pendergrass et al., 2018; Thorsen et al., 2018; Kramer et al., 2019b; Smith et al., 2020). Compared to the partial radiative perturbation method (e.g., Wetherald and Manabe, 1988), which is precise but computationally expensive, the kernel method deploys a set of precalculated radiative kernels with simple arithmetic multiplications in feedback quantification and thus is computationally highly efficient, which has greatly facilitated the analysis of radiative feedbacks in global climate models (GCM) (e.g., Soden et al., 2008; Jonko et al., 2012; Vial et al., 2013; Zhang and Huang, 2014; Soden and Held, 2006; Dong et al., 2020; Zelinka et al., 2020; Chao and Dessler, 2021), as well as in observations (e.g., Dessler, 2010; Kolly and Huang, 2018; Zhang et al., 2019; Huang et al., 2021a). These analyses have helped dissect and understand the climate sensitivity differences among the GCMs, such as those in Coupled Model Intercomparison Projects, CMIP5 (Taylor et al., 2012) and CMIP6 (Eyring et al., 2016). For example, Zelinka et al. (2020) attributed the higher climate sensitivity in the CMIP6 models to their more positive extratropical cloud feedback. The kernel-enabled feedback analyses have also provided insights in the energetics of the climate variations such as the El Nino and Southern Oscillation (ENSO, e.g., Dessler et al., 2010; Kolly & Huang 2018; Huang et al. 2021a), the Madden-Julian Oscillation (MJO, e.g., Zhang et al. 2019) and the Arctic sea ice interannual variability (e.g., Huang et al., 2019), despite the approximation nature of the kernel method and the known limits of its accuracy (e.g., Colman and Mcavaney, 1997; Huang and Huang, 2021).

Multiple sets of radiative kernels have been developed to date, using different radiation codes and based on different atmospheric state datasets ranging from GCMs to global reanalysis and satellite datasets, for both non-cloud variables (e.g., Soden and Held, 2006; Shell et al., 2008; Huang et al., 2017; Thorsen et al., 2018; Bright and O'halloran, 2019; Donohoe et al., 2020) and cloud properties (e.g., Zelinka et al., 2012; Zhou et al., 2013; Yue et al., 2016; Zhang et al., 2021; Zhou et al., 2022). As the conventional feedback analyses are mostly concerned with the radiation energy budget change at the TOA, most existing kernels have been developed and tested to address that need, i.e., to measure the feedback contributions to the TOA radiation changes. Although the radiative sensitivity depends on the atmospheric states as well as the radiative transfer codes used to compute the kernel values (e.g., Collins et al., 2006; Huang and Wang, 2019; Pincus et al., 2020), it has been noted that the global mean TOA feedback quantification is insensitive to which kernel dataset is used, as the diagnosed feedback values are close to each other when measured by different kernel datasets (e.g., Soden et al., 2008; Jonko et al., 2012; Vial et al., 2013). However, as there is increasing interest in regional climate change and associated feedback (e.g., Kolly and Huang, 2018; Huang et al., 2019; Zhang et al. 2019), it becomes important to know how the kernels (dis)agree at regional scales. The generation of the global radiative kernels usually requires radiative transfer computation based on a large number of instantaneous atmospheric profiles. Due to this computational cost, many kernel datasets are generated based on the atmospheric data from an arbitrary calendar year. Given the known interannual climate differences, e.g., between El Niño to La Niña years, this calls into question whether the kernels may differ in important ways for regional feedback assessments.

On the other hand, fewer feedback studies have addressed the surface radiation budget, although its importance has been recognized for such problems as the precipitation change (Previdi, 2010; Pendergrass and Hartmann, 2014; Myhre et al., 2018) and oceanic energy transport (e.g., Zhang and Huang, 2014; Huang et al., 2017). The surface budget analysis requires the use of surface kernels, which are not always available from the published kernel datasets. Few of them have been subject to inter-comparisons or rigorous validation. As explained below in this paper, the computation and use of them require different care than the TOA kernels. Possibly due to the lack of such recognition, there exist considerable discrepancies between the existing surface kernels and some surface budget-centered analyses reported alarmingly large non-closure in their radiation budget analyses (e.g., Vargas Zeppetello et al., 2019), calling into question the validity of kernel method for surface radiation budget analysis. Hence, we are motivated to examine the radiative sensitivity quantified by different kernels, especially for the surface budget.

In this work, we produce a new set of radiative kernels for both the TOA and surface radiation fluxes based on the fifth generation European Center for Medium-Range Weather Forecasts atmospheric reanalysis (ERA5, Hersbach et al., 2020), which demonstrates superior accuracy in the quantification of various atmospheric states, and document the key considerations in the kernel computation procedure. We intercompare the kernels computed from ERA5 to the other previously generated ones, and investigate the interannual variation of the kernel values due to their atmospheric state dependency. In addition, applying a selected sets of kernels to analyzing the feedback in the CMIP6 models, we intercompare the discrepancies in quantified feedbacks across the GCMs and across different kernels.

## 2. Construction of ERA5 radiative kernels

### 2.1 Radiative transfer model and atmospheric dataset

We use the GCM version of the rapid radiative transfer model (RRTMG) (Mlawer et al., 1997) to calculate the radiative kernels. RRTMG conducts radiative transfer calculations in 16 longwave (LW) spectral bands and 14 shortwave (SW) bands. The accuracy of this model has been extensively validated against the line-by-line calculations (e.g., Collins et al, 2006).

Input data required by RRTMG, including surface pressure, skin temperature, air temperature, water vapor, albedo, ozone concentration, cloud fraction, cloud liquid water content and cloud ice content, are taken from the instantaneous (as opposed to monthly mean) data of the ERA5 reanalysis, with a horizontal resolution of 2.5 degree by 2.5 degree and 37 vertical pressure levels between 1 hPa and 1000 hPa. To ensure the accuracy of radiative kernels in upper atmosphere (Smith et al., 2020), we patch five layers of the U.S. standard profile above 1 hPa in the LW calculations. Other required input variables, such as the effective radii of cloud liquid droplet and ice crystal are taken from the 3-hourly synoptic TOA and surface fluxes and cloud product of the Clouds and Earth's Radiant Energy System (CERES) (Doelling et al., 2013) with a horizontal resolution of 1 degree and then interpolated to the same resolution as the ERA5 data (2.5 degree). A random cloud overlapping scheme is used in our all-sky calculation. Sensitivity tests have been conducted to determine the necessary temporal sampling for a proper representation of the diurnal cycle and 6-hourly and 3-hourly instantaneous profiles are adopted for LW and SW radiative transfer calculations, respectively, to limit the root mean squared error of the computed diurnal mean flux biases to less than one percent.

### 2.2 Radiative kernel computation

Radiative kernels in essence measure the change of radiative flux to unit perturbation of atmospheric variables, i.e., $\frac{\partial R}{\partial X}$, where $R$ is either the upwelling irradiance flux at the TOA or upwelling/downwelling irradiance flux at the surface; $X$ represents the aforementioned feedback variables; $K_X$ is the radiative kernel of variable $X$. Note that for each radiative flux, $K_X$ varies with the time, geographic and vertical locations of the perturbed variable and is in general a 4-dimensional (4-D) data array. Note also that all radiative fluxes and kernel values are defined as downward positive.

Following the previous studies, we compute non-cloud radiative kernels including the LW kernels of surface temperature ($T_s$), air temperature ($T_a$), and water vapor ($WV\ LW$), and the SW kernels of surface albedo ($ALB$) and water vapor ($WV\ SW$). To calculate the kernels, we use the partial radiative perturbation experiments, conducting two radiative transfer simulations, one without perturbation (control run) and the other with a perturbation of one atmospheric variable; the difference between these two simulations is used to calculate radiative kernel value. In both experiments, the upward, downward and net radiative fluxes at the TOA and surface are saved at each time instance and location. Then $\Delta R_0$ can be obtained by differencing the saved radiative fluxes between the perturbed and unperturbed experiments. Dividing $\Delta R_0$ with the perturbation of variable $X$ ($\Delta X_0$), the instantaneous radiative kernel $K_X$ is calculated as

$$K_X = \frac{\Delta R_0}{\Delta X_0} \qquad (1)$$

Applying such perturbation computations to all the relevant variables (see Appendix for a detailed discussion of the procedure), we obtain instantaneous radiative kernels of these dimensionalities: the surface temperature and albedo kernels are 3-D arrays (time, latitude|73, longitude|144), and the air temperature and water vapor kernels are 4-D arrays (time, level|37, latitude|73, longitude|144).

To account for possible interannual variability of the radiative kernel values, we compute the kernels using atmospheric data of five calendar years: from year 2011 to 2015. Among these years, 2011 is a strong La Niña year, 2015 is a strong El Niño year. Monthly or annual mean kernels are then averaged from the instantaneous computations. For example, the LW annual mean kernel of 2011 is obtained as $K = \frac{1}{365*4}\sum_{i=1}^{365*4} K_i$ (365 is the number of days of a year and 4 is because 6-hourly data are used for LW calculations) and the SW kernels, $K = \frac{1}{365*8}\sum_{i=1}^{365*8} K_i$ (8 is because 3-hourly data are used for SW calculations), where the index $i$ represents the time slices included in the averaging. The analyses in this work are based on multi-year mean kernels if not otherwise stated.

## 3. Characterization of ERA5 kernels

In this section, we first present the all-sky TOA and surface radiative sensitivity kernels quantified from the ERA5 in Figure 1 to 4 (the clear-sky kernels as well as the atmospheric kernels are shown in Figure S1-S4 for interested readers). Then, we compare ERA5 kernels with the other kernel datasets and we examine the interannual variability of the ERA5 kernel values, due to the dependency of radiative sensitivity on the background atmospheric state.

### 3.1 Distribution of radiative sensitivity

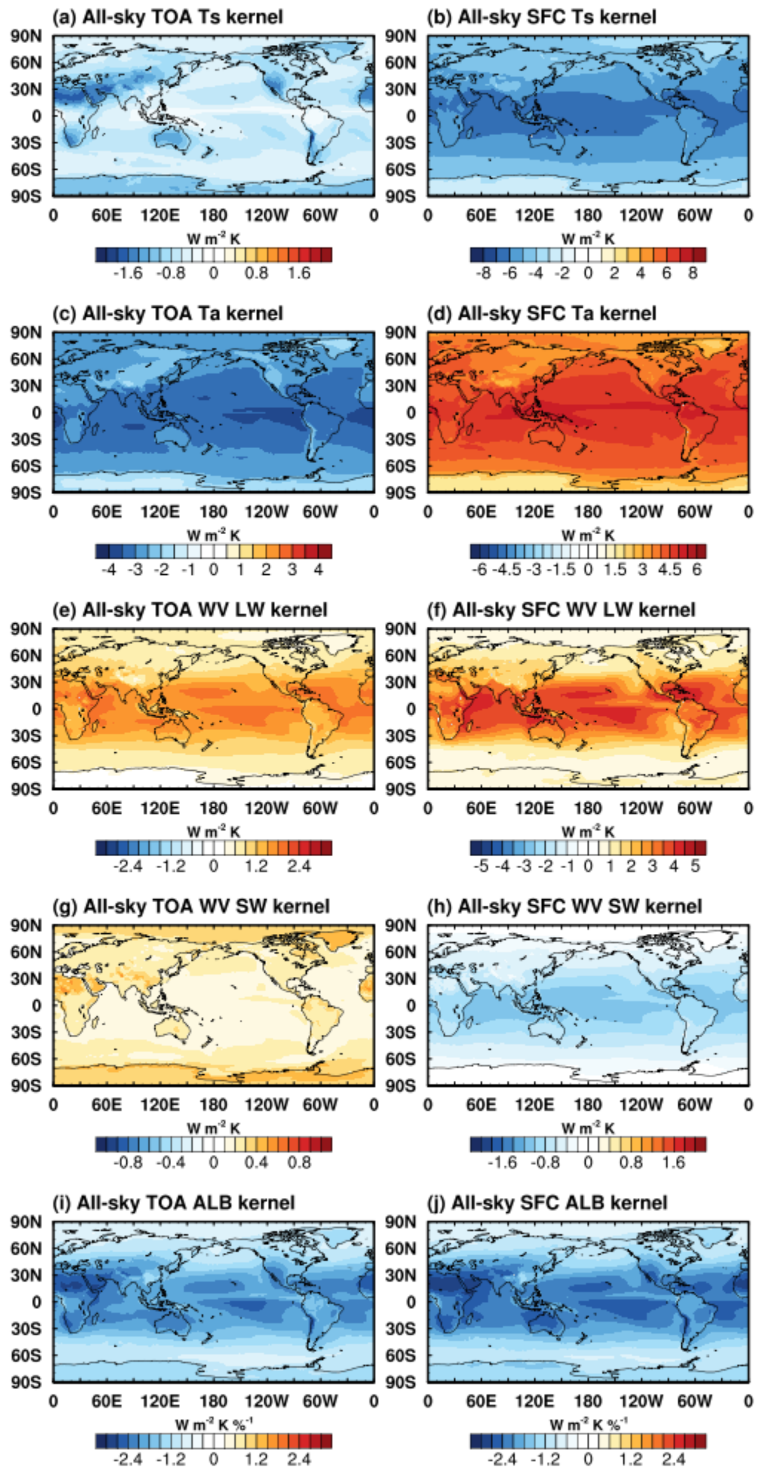


Figure 1. All-sky (left) TOA and (right) surface ERA5 kernels of (a, b) surface temperature ($T_s$), (c, d) air temperature ($T_a$), (e, f) water vapor longwave ($WV\ LW$), (g, h) water vapor shortwave ($WV\ SW$) and (i, j) surface albedo ($ALB$). Note that for $T_a$, $WV\ LW$, and $WV\ SW$ kernels, vertically integrated values are shown, which represents the sensitivity of radiative flux to a whole-column atmospheric perturbation.

Figure 1 summarizes the spatial distribution of all-sky ERA5 kernels for TOA and surface and Figure 2 illustrates the vertical cross-sections of zonal mean air temperature, water vapor LW and water vapor SW kernels in all-sky (see Figure S1 and S2 for results in clear-sky). For surface temperature kernel, an increase of surface temperature leads to more upwelling longwave radiation (i.e., OLR) both at the surface and TOA, therefore the kernel is negative. The TOA flux sensitivity in clear-sky (Figure S1a) is stronger than that in all-sky (Figure 1a) due to the absence of cloud, and the value increases with latitude, due to the decreasing concentration of water vapor from the tropics to the poles. The all-sky TOA sensitivity is strongly influenced by clouds, showing, for example, the fingerprint of the ITCZ in the tropical oceans (Figure 1a). The locations with less atmospheric absorption due to less water vapor or cloud, e.g., in the Tibetan Plateau and Sahara Desert regions, show relatively stronger sensitivity (Figure 1a). For the surface flux kernels, the increase of surface temperature enhances the upward emission according to the Planck function and thus the distribution follows that of surface temperature in both clear-sky and all-sky (Figure 1b).

For air temperature kernel, the increase of air temperature increases the OLR at TOA and also the downwelling flux at surface, so the TOA and surface kernels take negative and positive signs, respectively. The TOA kernel has maximum values in the tropics, due to the higher air temperature (Planck function) and more abundant cloud and water vapor (higher emissivity) there, and generally decreases in magnitude with latitude (Figure 1c). Unlike the TOA flux kernel, which shows comparable sensitivity to air temperature at nearly all vertical levels, the surface flux is mainly sensitive to the bottom layers (Figure 2b).

For water vapor LW kernel, an increase of water vapor reduces OLR at TOA and increases downwelling radiation at surface, so that the TOA and surface kernels are both positive in sign. The vertically integrated kernel values (Figure 1e and f) generally follow the temperature distribution, for example, decreasing in magnitude with latitude. In both cases, the kernel magnitude is dampened by clouds in all-sky. The vertically resolved kernels show maximum sensitivity of TOA flux to the upper troposphere (Figure 2c) and maximum sensitivity of surface flux to the bottom layers (Figure 2d), respectively. In terms of the atmospheric radiation (the convergence of the TOA and surface radiation fluxes in the atmosphere), the increase in water vapor concentration absorbs more LW in the upper troposphere than what it emits but the opposite is true in the lower troposphere (Figure S4c). Such features were discussed in previous works (e.g., Huang et al. 2007).

For water vapor SW kernel, an increase of water vapor absorbs solar radiation and thus reduces both the upwelling (reflected) SW flux at TOA and the downwelling SW flux at surface. As a result, the two kernels take positive and negative signs, respectively. Note the magnitude of the SW kernels is much weaker than that of the LW kernels, because water vapor absorbs the LW flux more significantly than the SW flux. One noticeable feature of the TOA kernel in clear-sky (Figure S1g) is that the magnitude over the land is stronger than that over the ocean, because the relatively higher albedo over the land reflects more SW radiation and thus enhances the absorption by the water vapor in the atmosphere. For this reason, over reflective surfaces such as the Sahara Desert and Tibetan Plateau, as well as the Poles, the sensitivity is maximized. Unlike the TOA kernel, the distribution of surface kernel follows the distribution of background water vapor concentration, with noticeable dampening by clouds (Figure 1h and 2f).

For surface albedo kernel, an increase of surface albedo leads to more upwelling (reflected) SW flux both at surface and TOA; therefore, the kernel is of negative sign. In clear-sky, the sensitivity strength follows the pattern of solar insolation, with some local maxima, e.g., in the Sahara Desert and Tibetan Plateau (Figure S1i and j) due to the relatively lower water vapor concentration. In all-sky, the distribution is again influenced by cloud patterns; for example, in the ITCZ region, the strength is much reduced as clouds reduce the solar radiation reaching the surface and thus the sensitivity to surface albedo change (Figure 1i and j).

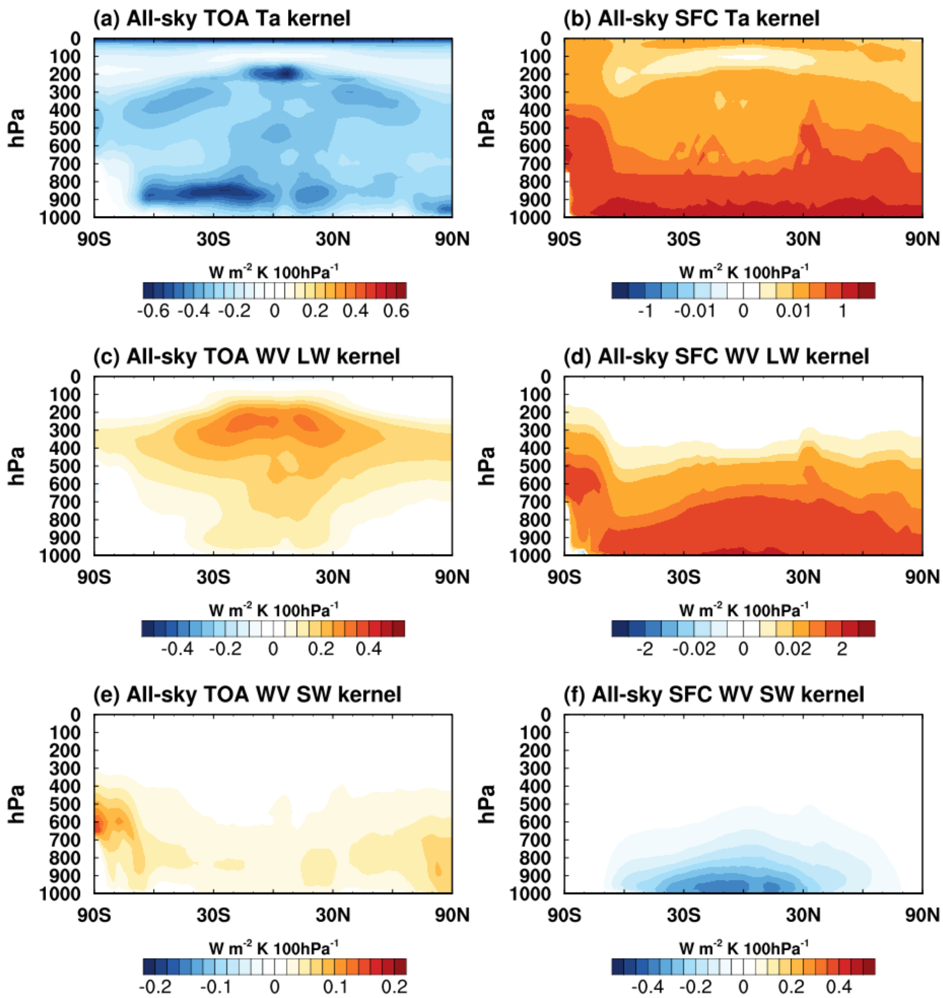


Figure 2. All-sky (left) TOA and (right) surface ERA5 vertically resolved and zonally averaged kernels of (a, b) air temperature ($T_a$), (c, d) water vapor longwave ($WV\ LW$) and (e, f) water vapor shortwave ($WV\ SW$), units: W m$^{-2}$ K$^{-1}$ 100hPa$^{-1}$. Note nonlinear colorbars used for surface air temperature and water vapor LW kernels.

### 3.2 Comparison of ERA5 kernels with other datasets

To examine the discrepancies between different kernel datasets, we select six previously published ones for comparison. Table 1 summarizes their resolutions and the atmospheric datasets based on which they are computed, including the GCMs: GFDL (Soden et al., 2008), CAM3 (Shell et al., 2008), CAM5 (Pendergrass et al., 2018), and HadGEM3 (Smith et al., 2020), a global reanalysis: ERAi (Huang et al., 2017), and satellite observations: CloudSat/CALIPSO (Kramer et al., 2019b). This list is meant to be representative instead of exhaustive.

Table 1. Summary of radiative kernels compared in this work. Datasets with * only have TOA kernels.

| Radiative kernels | Horizontal resolution (lat*lon) | Vertical resolution | Reference |
|---|---|---|---|
| GFDL* | 2x2.5 | 17 (pressure level) | Soden et al., 2008 |
| CAM3* | 2.8x2.8 | 17 (pressure level) | Shell et al., 2008 |
| ERAi | 2.5x2.5 | 24 (pressure level) | Huang et al., 2017 |
| CAM5 | 0.94x1.25 | 30 (hybrid level) or 17 (pressure level) | Pendergrass et al., 2018 |
| CloudSat | 2x2.5 | 17 (pressure level) | Kramer et al., 2019b |
| HadGEM3 | 1.25x1.9 | 85 (hybrid level) or 19 (pressure level) | Smith et al., 2020 |
| ERA5 | 2.5x2.5 | 37 (pressure level) | This study |

To facilitate an intercomparison, these kernel datasets are interpolated to the same horizontal and vertical resolutions as those of the ERA5 kernel when illustrated in Figure 3 and 4 (see Figure S5 and S6 for clear-sky) and are uploaded to the same data repository of ERA5 kernels. Note that the CAM5 and HadGEM3 kernels have two versions, with one defined at the raw hybrid levels and the other interpolated to pressure levels. To retain the accuracy of them as much as possible, the hybrid level version is used for the interpolation and comparison in Figures 3 and 4, while in Section 4, the pressure level version is used for quantifying the feedbacks of CMIP6 models. The GFDL and CAM3 kernels are only available for TOA fluxes and are excluded for surface kernel comparisons.

Here we use the standard deviation ($std$) and its normalized value ($std^*$) to measure the spread of the inter-kernel dataset differences:

$$std_X = \sqrt{\frac{1}{n-1}\sum_{i=1}^{n}\left(K_X^i - \overline{K_X}\right)^2} \quad (2)$$

$$std_X^* = \frac{std_X}{\overline{K_X}} * 100 \quad (3)$$

where $n$ is the total number of kernel datasets. $K_X^i$ is radiative kernel of variable $X$ from the $i^{th}$ dataset. $\overline{K_X}$ is the multi-dataset mean of radiative kernel $K_X$. Note that $\overline{K_X}$ does not represent the "truth" value, but a reference value used to measure the spread of multi-kernel values. The vertically integrated and the vertically resolved but zonally averaged distributions of fractional discrepancy ($std^*$) are shown in Figures 3 and 4, respectively. The zonal mean kernel values from respective multi-datasets are shown in line plots in Figure 3 and 4. Note that some kernels exhibit abnormal values, such as the surface and air temperature kernel of the surface flux in the CAM5 and CloudSat kernels (see Appendix Figure A2), indicating inconsistent computation of their values, and thus are excluded in the corresponding $std_X^*$ statistics in Figures 3 and 4. See more discussions in Appendix.

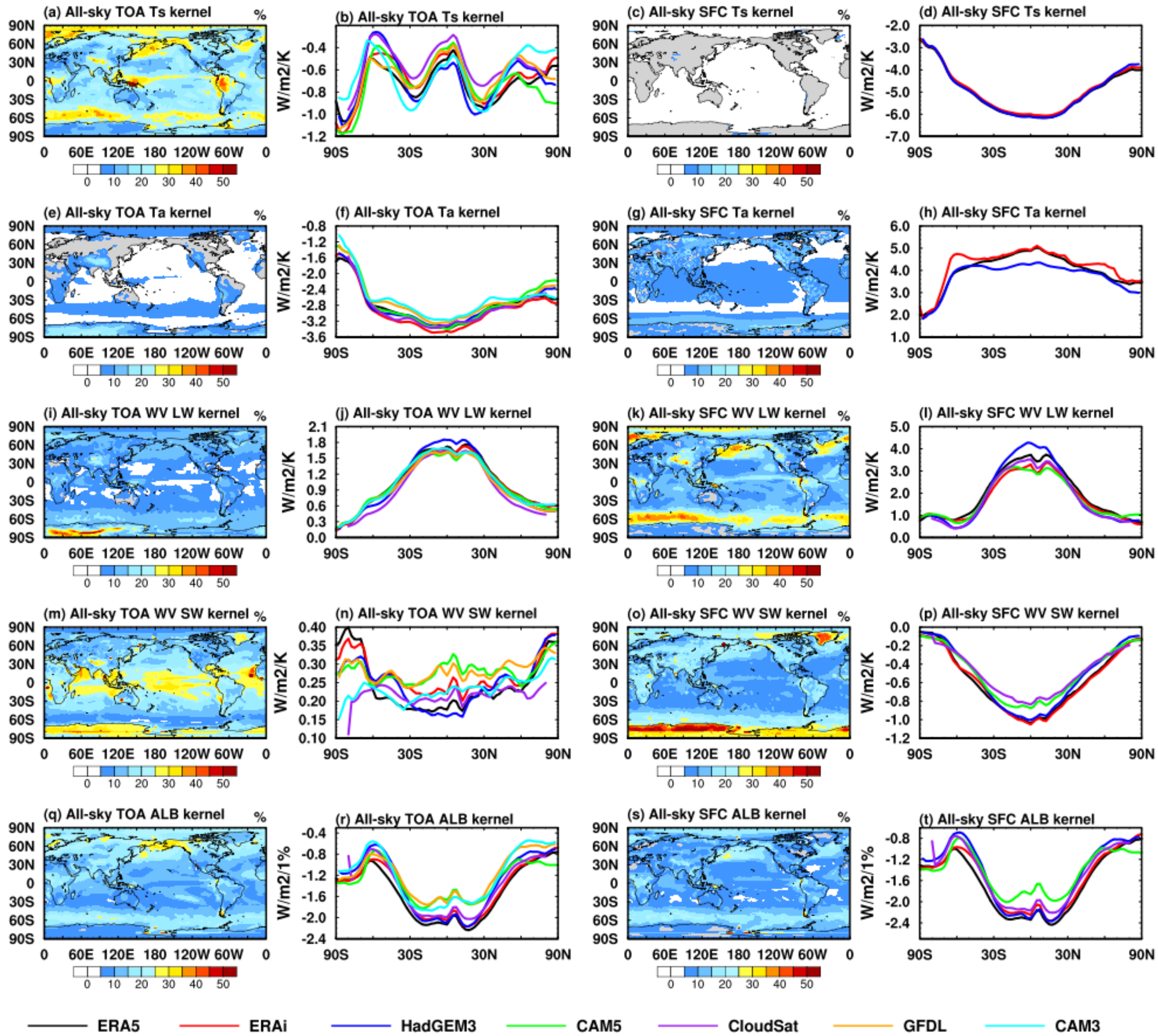


Figure 3. (contour plot) fraction discrepancies as measured by the normalized standard deviation of the kernels by Eq. (3) and (line plot) zonal mean distribution of multi-kernels in all-sky.

The comparisons identify the following relatively larger differences in kernel values. Among the TOA kernels, the surface temperature and albedo kernels show relatively large discrepancies in the Arctic, Southern Ocean and over some continental regions in the tropics in all-sky (Figure 3a and q), with the maximum discrepancy exceeding 30%; the air temperature kernel shows larger discrepancies in the lower troposphere and tropical tropopause region (Figure 4a); these kernel differences are likely due to the differences in cloud fields. The water vapor LW kernel also shows noticeable fractional biases, for example, over the Antarctic region (Figure 3i and 4e). The water vapor SW kernel shows differences in the tropical mid-troposphere and over Antarctic in both clear-sky and all-sky (Figure 4i and S6i), leading to strong variations in the vertical integration of sensitivity (Figure 3m and S5m), with a spread exceeding 30%. The noticeable periodic equatorial pattern in Figure S5m is caused by the CAM3 kernel, likely due to a coarser temporal resolution that does not well resolve the diurnal cycle of solar insolation in the kernel computation.

For the surface kernels, the most prominent differences exist in SW radiative kernels (Figure 3 and 4), especially in the polar regions. The discrepancy in the water vapor SW kernel reaches 30% for vertically integrated values (Figure 3o), with noticeable biases through the troposphere (Figure 4k). The surface albedo kernel differences are much larger in all-sky than that in clear-sky (Figure 3 and S5), indicating that the cause is in cloud fields, and are also noticeable in the Arctic region due to sea ice variations (Figure 3s). In the LW, the water vapor kernels exhibit noticeable differences in the Central Pacific, Southern Ocean and Arctic in all-sky (Figure 3k), where again the difference in cloud field is likely the cause. The air temperature kernels show noticeable discrepancies in the bottom layers (Figure 4d), which may be caused by inconsistency in the kernel computation and vertical resolutions (see the discussions in Appendix).

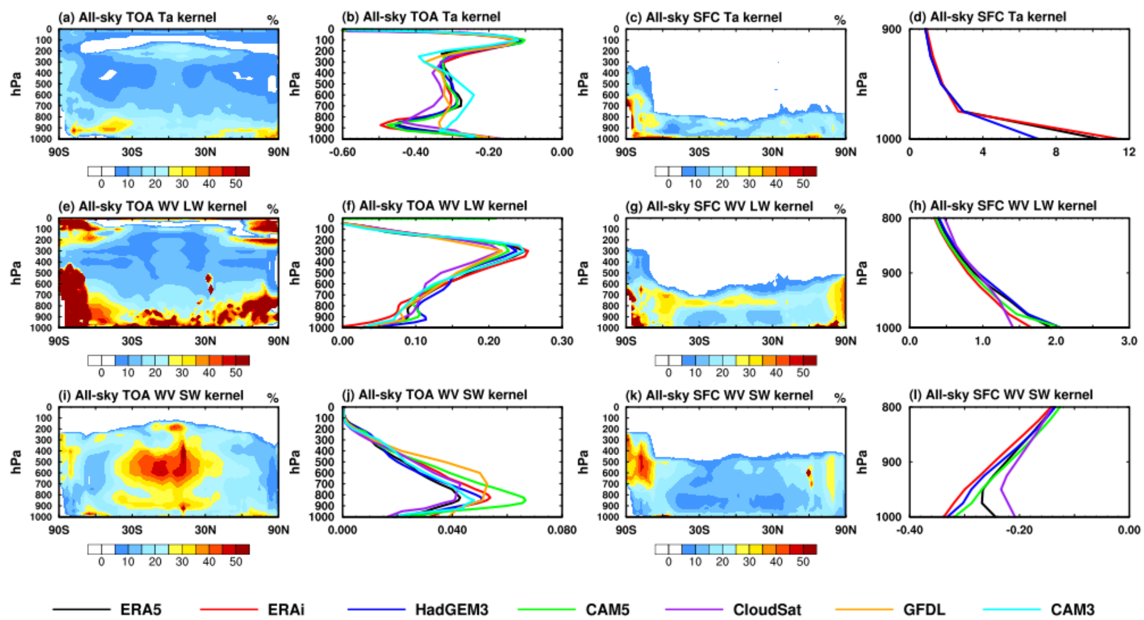


Figure 4. (contour plot) Cross-section of fraction discrepancies of the radiative kernels, (line plot) global mean vertically resolved kernels from multi-datasets in all-sky.

In summary, the differences among radiative kernel datasets are generally smaller in clear-sky than in all-sky and in most cases, are mostly within 10%. However, there are some notable regional discrepancies, for example, in the surface temperature kernel in the tropics (Figure 3a), in the surface albedo kernel in the Arctic (Figure 3q), and in the water vapor SW kernel in the Antarctic region (Figure 3m). As different kernel datasets are calculated using different data sources, the discrepancies detected here are likely due to the state-dependency in the kernels, which differ between the kernel datasets. To ascertain the state-dependency-caused kernel uncertainty, we next examine the ERA5 kernels computed from different years, i.e., from different atmospheric states, to investigate how much difference in radiative sensitivity can result from the change in atmospheric state.

### 3.3 Interannual variation of kernel values

The intercomparison above identified several prominent inter-dataset differences in the kernel values. For example, there are noticeable differences in the values of surface temperature, albedo and water vapor kernels in the Central Pacific and Arctic region. One possible reason that may account for such differences is the atmospheric state-dependency of the kernel values. Besides the inter-model differences in the different GCM climatology, interannual variations of the atmospheric states, such as cloudiness variations in the Central Pacific region during the ENSO cycle, may affect the radiative sensitivity as some radiative kernels are calculated using one arbitrary year's data. To test this hypothesis, we use the ENSO and sea ice loss cases to demonstrate the changes in radiative sensitivity with a focus on Central Pacific and Arctic region, respectively. In the ENSO case, the variation is defined as the difference in annual mean kernel values between 2015 and 5-year mean (from 2011 to 2015), which have the annual mean sea surface temperature anomalies in the Niño 3.4 region (5N-5S, 190-240E) over +2.0K. In the sea ice loss case, the variation is calculated as the difference in September between year 2012 and 2013, as the sea ice cover in 2012 was reported to be the lowest level in the satellite observation era. In addition, we further show the comparison between ERA5 and ERAi kernels (in Figure 5), which was also calculated by RRTMG and averaged from 5 years' calculations (2008-2012), to compare the inter-kernel difference and interannual difference in kernel values.

To save space, here we only highlight the most prominent differences. Figure 5a-c show the differences in skin temperature, total column water vapor and total cloud cover due to ENSO and Figure 5d-f summarize the corresponding differences in all-sky TOA kernels. As the skin temperature in the Central Pacific warms over 2K (Figure 5a) during ENSO, the increases in water vapor concentration and cloud fraction (Figure 5b and c) reduce the sensitivity of TOA flux to surface temperature change by about 0.2 W $m^{-2}$ $K^{-1}$ (about 33%) (Figure 5d). The moistening in the Central Pacific (Figure 5b) enhances the TOA water vapor LW sensitivity in clear-sky (Figure S7b), while in all-sky the enhanced convection and associated total cloud cover in this region lead to a weakened TOA water vapor LW radiative sensitivity (Figure 5e) despite the moist anomaly, and the decrease is almost contributed from the whole troposphere (Figure S8c). The water vapor SW kernel discrepancy is less pronounced (Figure 5f).

Comparing the 5-year averaged all-sky ERA5 and ERAi kernels, we find that the atmospheric state differences also exist between the atmospheric datasets on which the kernels are computed from. For example, the ERA5 shows similar, but less pronounced, warming anomalies in sea surface temperature in the Central Pacific compared to ERAi, partly due to the strong El Nino year (2015) included in the ERA5 dataset. ERA5 data also shows more water vapor and cloud cover (Figure 5h and i). As a result, the surface temperature kernel computed from ERA5 shows less TOA radiative sensitivity to surface temperature than that from ERAi. It is also noticed that the ERA5 water vapor SW kernel shows lower sensitivity and mainly comes from the contributions in mid-to-low troposphere (Figure S8f), which corresponds to the discrepancy noticed in Figure 4i. The clear-sky kernels are of much less differences (Figure S7), confirming that the difference in clouds is the main cause of the all-sky kernel differences, which also correspond to the discrepancies shown in the multi-kernel comparisons in Figure 3a, i, and m.

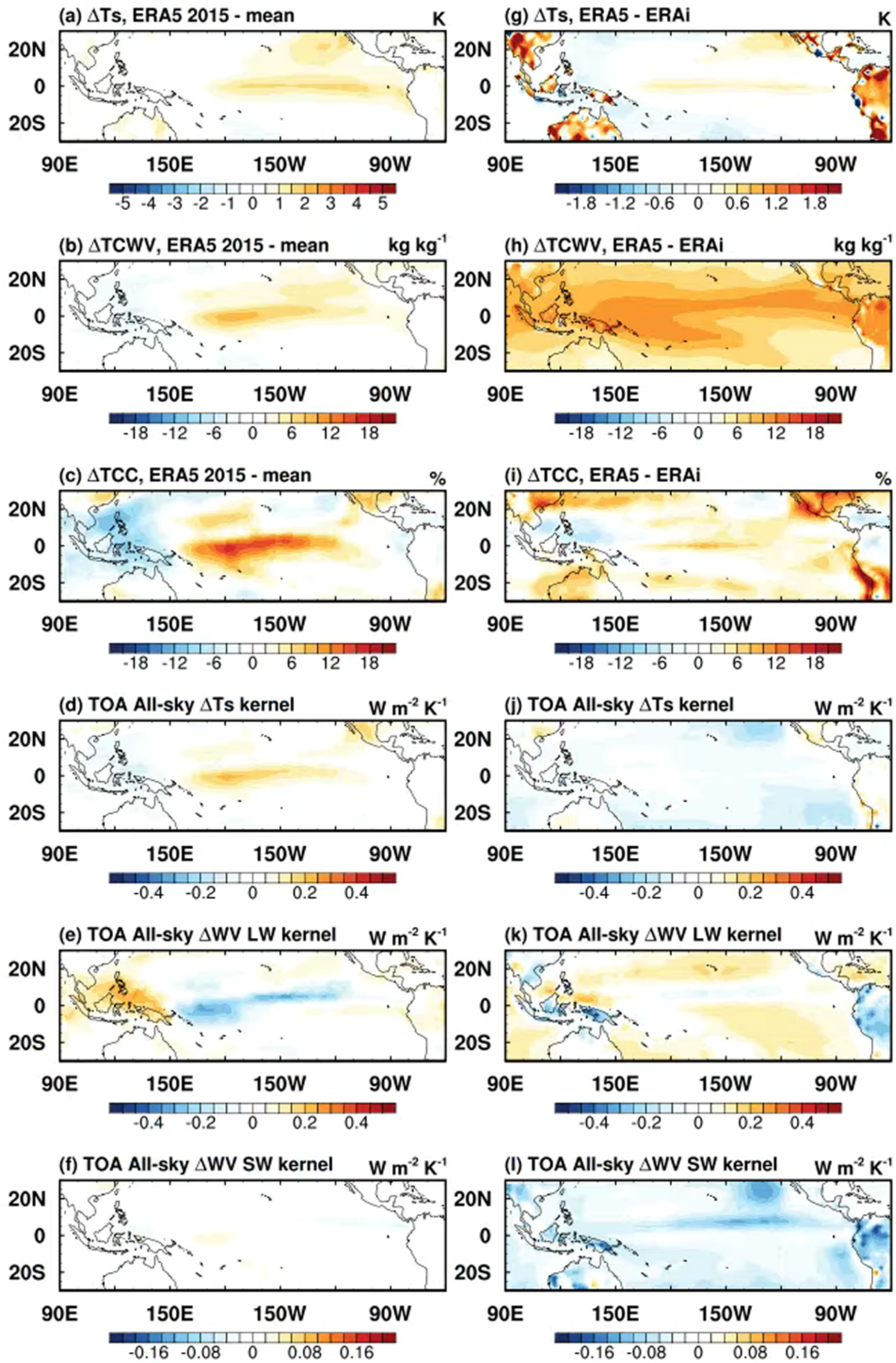


Figure 5. Differences in climate states and all-sky kernel values (left) between an arbitrary year (2015) and a 5-year mean of ERA5 and (right) between the 5-year means of ERA5 and ERAi datasets: (a, g) skin temperature, (b, h) total column water vapor (TCWV), (c, i) total cloud cover (TCC), (d, j) TOA skin temperature kernel, (e, k) TOA vertically integrated water vapor LW kernel and (f, l) TOA vertically integrated water vapor SW kernel.

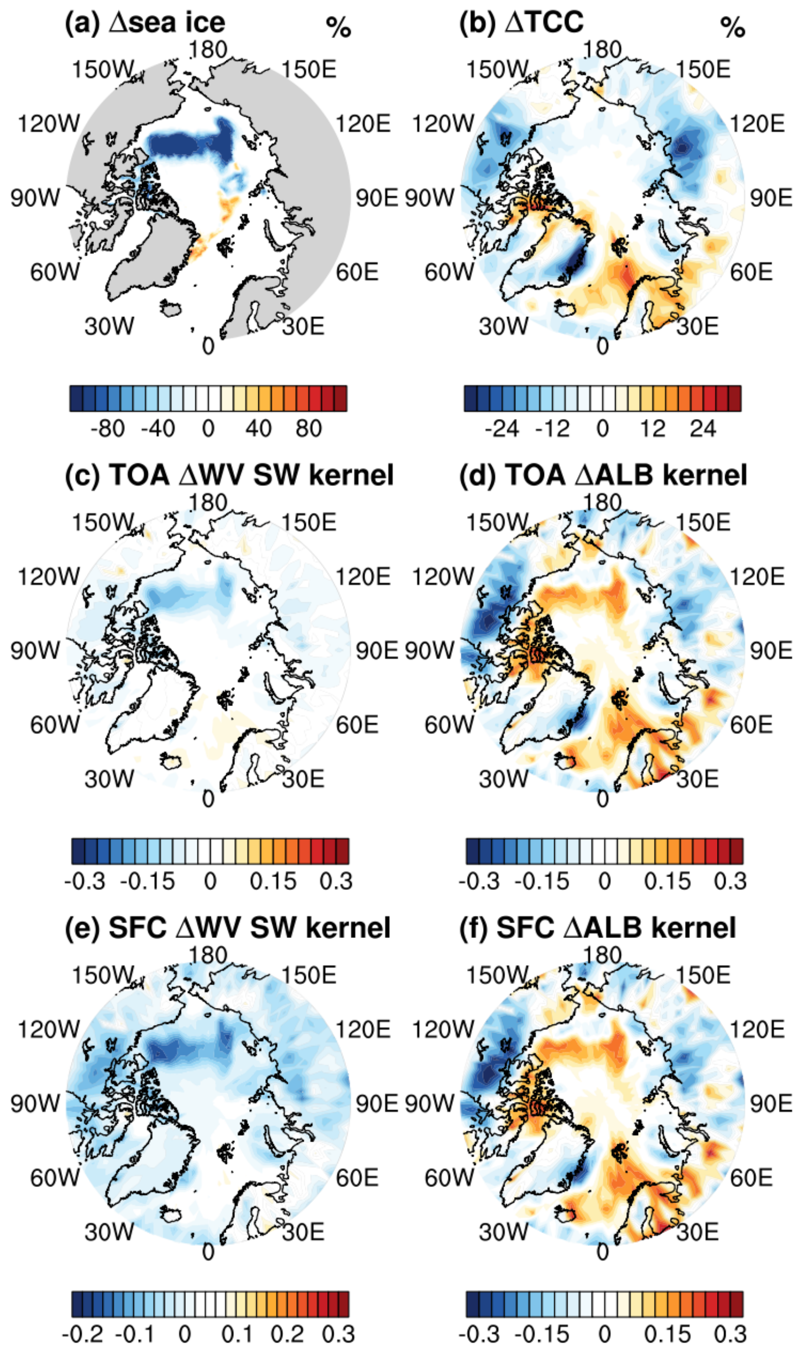


Figure 6. September differences between 2012 and 2013 in (a) sea ice concentration, (b) total cloud cover (TCC), and the differences in (c, e) water vapor SW kernel for TOA and surface fluxes, units: W $m^{-2}$ $K^{-1}$, (d, f) surface albedo kernel for TOA and surface fluxes, units: W $m^{-2}$ $1\%^{-1}$.

In the sea ice loss case, the reduction of sea ice in the Arctic region (Figure 6a) leads to a significant decrease of radiative sensitivity to surface albedo (Figure 6d and f), with the maximum difference exceeding 30%. The cloud cover change also contributes to changes in surface albedo kernel values due to the coupling effect between cloud and surface albedo (e.g., see Huang et al., 2021b), which for example is seen in the Siberia and to the west coastline of Europe. The change in sea ice also leads to a significant decrease in the TOA sensitivity and an increase of surface sensitivity to water vapor, respectively (Figure 6c and e), with the maximum changes exceeding 80% for surface. All these results confirm the state-dependency of radiative kernels (e.g., Riihelä et al., 2021).

In summary, these quantitatively large interannual differences, as well as their locations, affirm that some discrepancies between the radiative kernels are caused by the difference in atmospheric states and partly explain the inter-dataset kernel differences seen in Figure 3 and 4. Nevertheless, it ought to be noted that the differences are localized and because of that do not cause significant biases in the global mean feedback values (see Section 4). The results above also show that kernel values based on one arbitrary year may be regionally biased. If only one year's atmospheric profiles are used to generate radiative kernels, we recommend selecting a year without significant anomalies in atmospheric states, e.g., due to El Nino or severe sea ice loss.

## 4. Feedback quantification

In this section, we apply different kernels to quantifying the radiative feedbacks in one quadrupling $CO_2$ experiment (abrupt4x$CO_2$) of CMIP6 models. This experiment is selected because it has been used by a number of studies for forcing and feedback analyses (e.g., Zelinka et al., 2020), which we can compare our results to. The CMIP6 models used in this assessment are listed in Table2. Note that the standard outputs at 19 pressure levels from the models and correspondingly the kernel values, including CAM5 and HadGEM3, provided at the pressure levels are used in this section.

Table 2. Summary of CMIP6 models used in this study.

| Models | Horizontal resolution (lat*lon) | Vertical levels | Reference |
|---|---|---|---|
| CESM2 | 0.9*1.25 | 32 levels to 2.26 hPa | Danabasoglu et al. (2020) |
| CNRM-CM6-1 | 1.4*1.4 | 91 levels to 0.01hPa | Voldoire et al. (2019) |
| EC-Earth3 | 0.7*0.7 | 91 levels to 90 km | Döscher et al. (2022) |
| HadGEM3-GC31-LL | 1.25*1.875 | 85 levels to 85km | Williams et al. (2018) |
| IPSL-CM6A-LR | 1.3*2.5 | 79 levels to 80km | Boucher et al. (2020) |
| MPI-ESM1-2-LR | 1.875*1.875 | 47 levels to 0.01hPa | Mauritsen et al. (2019) |

### 4.1 Analysis procedure

To quantify the radiative feedbacks, data from two experiments as documented by Eyring et al. (2016) and Pincus et al. (2016) are used: abrupt4x$CO_2$, simulations with an instantaneous quadrupling of $CO_2$ concentration of year 1850, piClim-4x$CO_2$, simulations with SST and sea ice concentrations fixed at the climatology of pre-industrial control experiment and $CO_2$ concentration quadrupled. In each experiment, a 20-year period at the end of the simulation in each model is used. For example, in the models where the abrupt4xCO$_2$ simulation is longer than 150 years, the simulations from the last 20 years rather than those from years 131 to 150 are used for the calculation. Following the previous studies (e.g., Smith et al., 2020; Zelinka et al., 2020), radiative feedbacks are diagnosed using the difference of atmospheric variables between the abrupt4xCO$_2$ and piClim-4xCO$_2$ experiments. It is worth noting that the method used in this study is slightly different from that in Zelinka et al. (2020), in which piControl simulation was used as the climatology baseline and the feedbacks were integrated from the surface to the tropopause (as opposed to model top) to remove the rapid adjustment, although the quantitative differences in the global mean feedback values are small.

To detail the analysis procedure, firstly, all variables including radiative fluxes and atmospheric variables from CMIP6 models are interpolated to the horizontal and vertical resolution of the kernel itself. Notre that for CAM3, GFDL, CloudSat and CAM5 kernels, they only have 17 pressure levels which are two layers (1hPa and 5hPa) fewer than the CMIP6 standard model output. To address this issue, the contribution of the two missing layers is calculated using other kernels (e.g., ERA5) and found to have negligible effect on the global mean feedback value. Hence, when using these three kernels, the contributions from 10hPa above are ignored.

Secondly, the non-cloud radiative feedback of atmospheric variable $X$ ($\Delta R_X$) is calculated as:

$$\Delta R_X = K_X \cdot \Delta X \quad (4)$$

with units in W m$^{-2}$, where $K_X$ is the radiative kernel of variable $X$ and $\Delta X$ is the anomaly of $X$ measured by the difference between abrupt4xCO$_2$ and piClim-4xCO$_2$, and represents the anomalies of surface temperature ($\Delta T_S$), air temperature ($\Delta T_a$), water vapor ($\Delta WV$) and surface albedo ($\Delta ALB$). For the 2D radiative kernels (surface temperature and surface albedo), $K_X$ and $\Delta X$ have just single layer values and $\Delta R_X$ is simply the product of these two terms. For the 3D radiative kernels (air temperature and water vapor), both $K_X$ and $\Delta X$ are vectors of pressure levels and $\Delta R_X$ is the dot product of $K_X$ and $\Delta X$ and is integrated from the TOA to 1000hPa. Note that if $K_X$ is normalized with unit pressure thickness (e.g., W m$^{-2}$ K$^{-1}$ 100hPa$^{-1}$), the layer thickness must be taken into account when calculating $dR_X$. See Appendix for further discussion on the application of thickness-weighted kernels.

Finally, cloud feedbacks are diagnosed using the adjusted cloud-radiative forcing method (Shell et al., 2008). Here we compute the residual term in clear-sky as:

$$res^o = \sum \Delta R_X^o - \Delta R^o \qquad (5)$$

which represents the unexplained part of radiation budget change, and assuming the all-sky decomposition has the same non-closure residual, the cloud feedback is measured as

$$\Delta R_C = \Delta R - \sum \Delta R_X + res^o \qquad (6)$$

where the superscript $o$ represents clear-sky quantities. $\sum \Delta R_X^o$ and $\sum \Delta R_X$ are the sum of non-cloud feedbacks in clear-sky and all-sky, respectively, diagnosed by multiplying the radiative kernel with the atmospheric responses measured as the difference between abrupt4xCO$_2$ and piClim-4xCO$_2$ experiments. $\Delta R^o$ and $\Delta R$ are the total radiation change in clear-sky and all-sky, respectively, calculated as the difference in the GCM-simulated radiative fluxes between two experiments.

The feedback parameters, $\lambda_X$, in the units of W m$^{-2}$ K$^{-1}$, are then obtained by normalizing the feedback flux changes $\Delta R_X$ by the global mean surface temperature change $\Delta T_S$ in the abrupt4xCO$_2$ experiment:

$$\lambda_X = \Delta R_X / \Delta T_S \qquad (7)$$

### 4.2 TOA feedbacks

The residual term ($res^o$) measures the unexplained radiation change in the feedback analysis and provides a useful overall indication of the soundness of the feedback quantification. Figure 7 illustrates the residual term for the TOA flux decomposition when different kernels are used to diagnose the multi-model mean feedbacks. In terms of the global mean, all residual terms are of small magnitude, no matter which kernel dataset is used (Figure 8 and Table S1). However, there are some noticeable local residuals, especially for the SW budget, e.g., in the Arctic region and around the Antarctic continent where sea ice changes the most (mid-column in Figure 7). While the non-zero magnitude of the residual is partly due to nonlinearity in the radiation decomposition, e.g., possible coupling between surface albedo and water vapor (Huang et al., 2021b), the spread among the kernel results as evidenced by the line plots of Figure 7 is attributable to the discrepancies in the SW radiative kernels as revealed by the comparisons in Section 3. In the LW, the residual is generally small compared with the total feedback. In summary, the residual terms for the TOA budget are small in terms of the global mean feedback strengths, affirming the validity of the radiative kernels for feedback quantification. Here, we use the spatial root-mean square (RMS) of the residuals to quantify the regional biases, which are shown by the numbers on the right corner of each panel in Figure 7. For LW, results from ERA5, ERAi and CAM5 kernels show relatively smaller regional biases compared to those from HadGM3, CloudSat and CAM3 kernels. For SW, all kernel datasets have similar regional non-closures, for example, in the Polar regions (Figure 7 and 8). This is largely caused by the non-linearity in albedo feedback and also the coupling effect between water vapor and surface albedo feedbacks (Huang et al., 2021b; Block and Mauritsen, 2013). In summary, these results suggest that for the TOA feedback quantification, the performance of ERA5 kernel is comparable to the other datasets.

Figure 8 compares the spreads of feedback values resulted from the differences in kernels and those from the different projections of GCMs. In general, feedbacks from different kernel datasets overlap each other, even for cloud feedbacks, affirming a good consistency between the results computed from different kernel datasets. However, the spread across the GCMs is considerably larger, suggesting the overall feedback uncertainty is dominated by inter-model spread rather than the kernel uncertainty. The values of the feedbacks from each model and kernel datasets are shown in Table S1 and S2 for readers who are interested. These results are consistent with other published results. For example, compared with the results of Zelinka et al. (2020) based on the ERAi kernel, the kernel-diagnosed overall feedback parameter in the two results is -0.87 W m$^{-2}$ K$^{-1}$ and -0.85 W m$^{-2}$ K$^{-1}$ for the CNRM-CM6-1 model and -0.81 W m$^{-2}$ K$^{-1}$ and -0.84 W m$^{-2}$ K$^{-1}$ for the HadGEM3-GC3-LL model.

In summary, in terms of TOA feedback values, the inter-kernel differences lead to small uncertainty in the analyzed non-cloud feedbacks; the kernel-induced uncertainty in cloud feedback is relatively larger (Table S2), with the inter-kernel spread in cloud LW feedback almost equally from the spread in surface and air temperature feedback and water vapor LW feedback, and the inter-kernel spread in cloud SW feedback more from the spread in surface albedo feedback than from water vapor SW feedback (not shown); despite this, this uncertainty is considerably less than the inter-GCM cloud feedback spread.

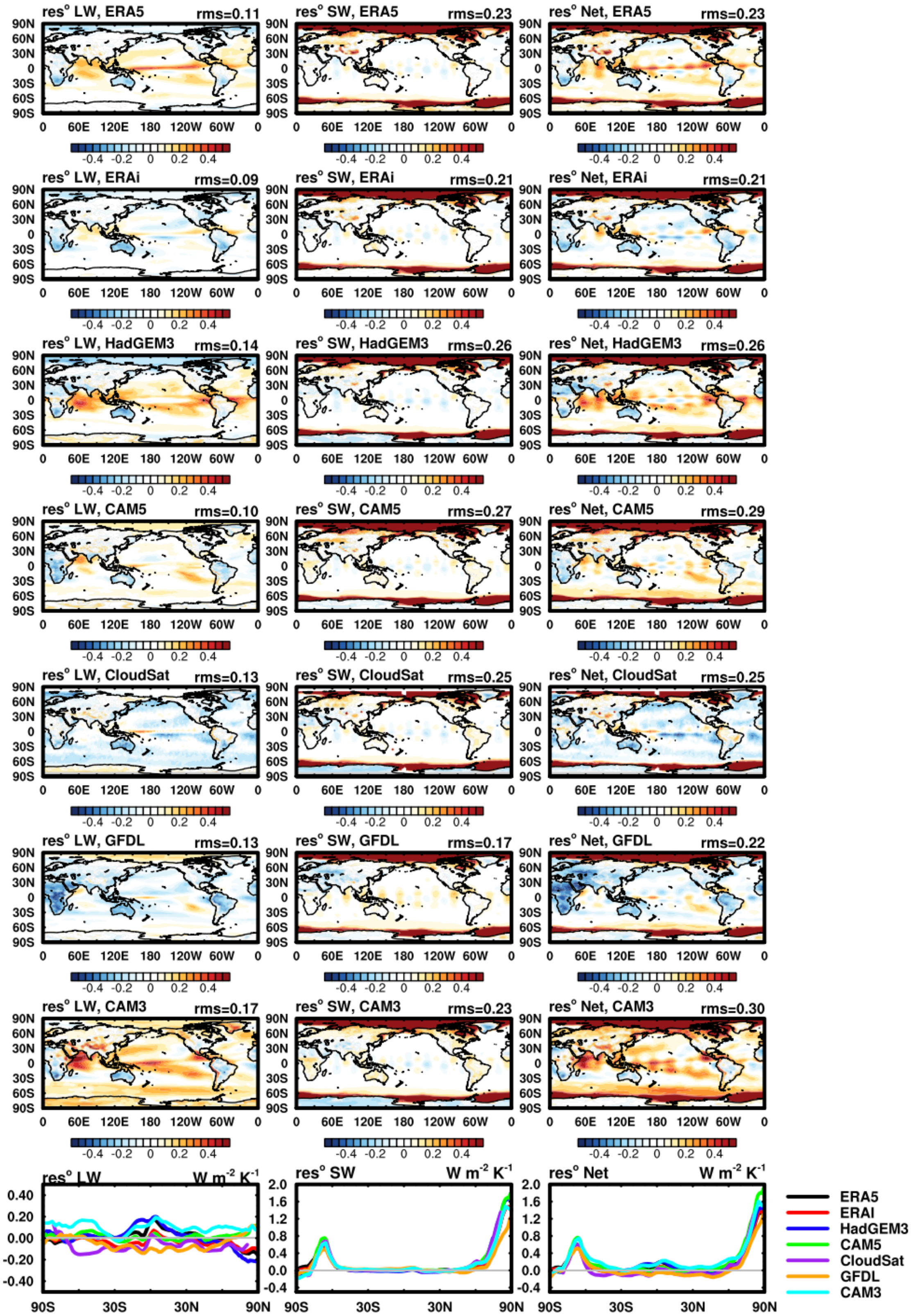
res° LW, ERA5 rms=0.11
res° SW, ERA5 rms=0.23
res° Net, ERA5 rms=0.23
res° LW, ERAi rms=0.09
res° SW, ERAi rms=0.21
res° Net, ERAi rms=0.21
res° LW, HadGEM3 rms=0.14
res° SW, HadGEM3 rms=0.26
res° Net, HadGEM3 rms=0.26
res° LW, CAM5 rms=0.10
res° SW, CAM5 rms=0.27
res° Net, CAM5 rms=0.29
res° LW, CloudSat rms=0.13
res° SW, CloudSat rms=0.25
res° Net, CloudSat rms=0.25
res° LW, GFDL rms=0.13
res° SW, GFDL rms=0.17
res° Net, GFDL rms=0.22
res° LW, CAM3 rms=0.17
res° SW, CAM3 rms=0.23
res° Net, CAM3 rms=0.30
res° LW W m-2 K-1
res° SW W m-2 K-1
res° Net W m-2 K-1
ERA5
ERAi
HadGEM3
CAM5
CloudSat
GFDL
CAM3

Figure 7. The residuals ($res^o$) in the multi-model mean TOA feedback decomposition when different kernels are used, (left column) LW, (mid-column) SW, (right-column) Net, the sum of LW and SW. The three line-plots in the bottom row are the zonal mean residuals. Numbers on the right corner in each panel are the spatial root-mean-square values.

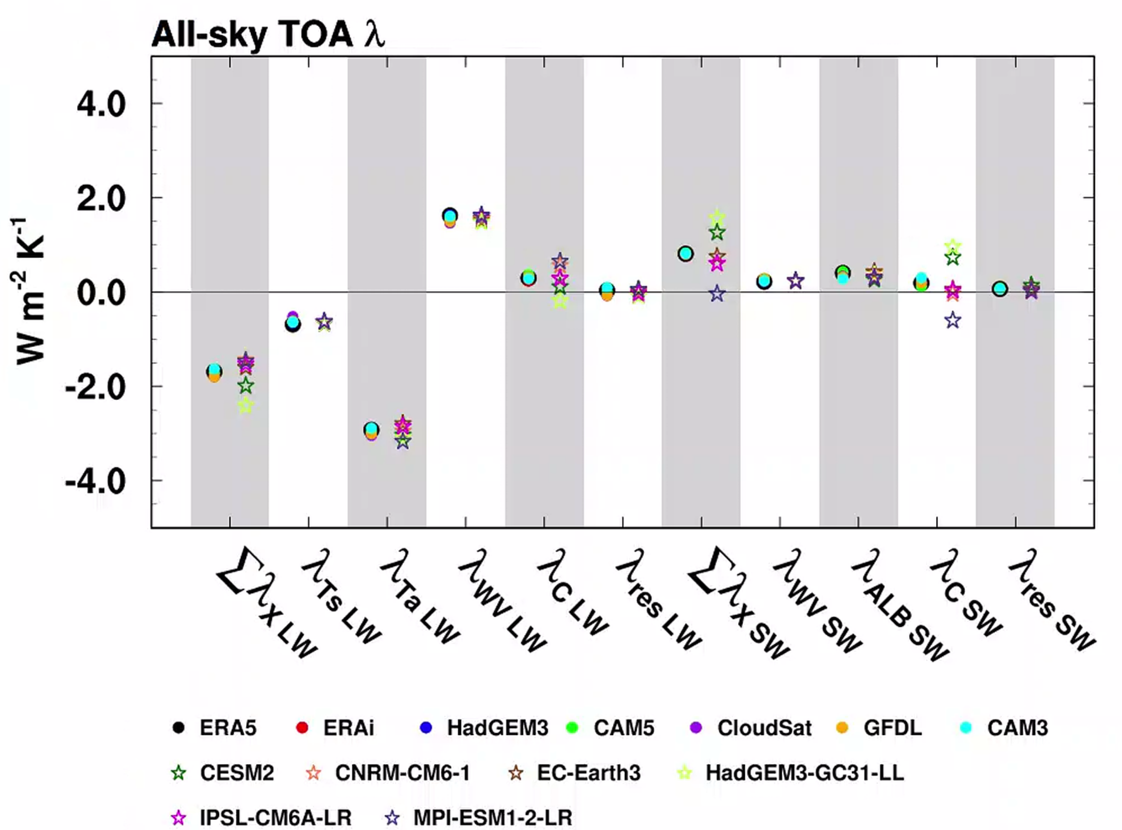


Figure 8. Global mean TOA feedback parameters in all-sky diagnosed by the kernels list in Table 1 across CMIP6 models. Dot marks represent multi-model mean values computed from different kernel datasets. Pentagrams represent the multi-kernel mean results computed from different GCMs.

### 4.3 Surface feedbacks

Next, we examine how the inter-kernel differences lead to uncertainty in the analyzed surface feedbacks.

Figure 9 shows the residual distribution. We find that when the ERA5 and ERAi kernels are used for the feedback analysis, the non-closure residual in the surface budget is comparable in magnitude to the TOA analysis. This suggests that the surface kernels afford a valid tool for the surface feedback analysis. However, some prominent biases are noticed for other kernel datasets. For example, the HadGEM3 kernels, show especially an underestimation in air temperature feedback, likely due to a biased sensitivity of the bottom atmospheric layer (see Appendix for more discussions). The sum of global mean surface and air temperature feedback parameter measured by the HadGEM3 kernel is around -3.70 W m$^{-2}$ K$^{-1}$ (Table S4, compared to around -1.0 W $m^{-2}$ $K^{-1}$ measured by the other kernels), and the non-closure residual is as large as -3.0 W $m^{-2}$ $K^{-1}$ (Table S2, compared to 0.1 W $m^{-2}$ $K^{-1}$ in the others). For this reason, the result from HadGEM3 kernel is excluded for the multi-kernel statistics in Figure 10, Table S3 and S4, but listed in a separate row for comparison. From either the spatial distribution of residual term or the spatial RMS residuals, the ERA5 kernel and ERAi kernel show a superior performance than other datasets. The use of ERA5 kernels may be advantageous for diagnosing the surface radiation budget, considering that ERA5 data is a newer version reanalysis dataset from ECMWF compared with ERAi and its data quality has been widely validated.

Figure 10 compares the inter-model and inter-kernel spreads for the surface feedbacks. Unlike the results for TOA, the inter-kernel spread can be as large as the inter-model spread, for example, in LW surface temperature feedback, air temperature feedback and water vapor feedback. The sum of air temperature and surface temperature feedbacks shows better consistency compared with the respective components, except for HadGEM3 kernel, which is due to the reason discussed in the Appendix - possibly wrong quantification of surface temperature effect. In SW, the multi-kernel results are close to each other, showing smaller inter-kernel spreads than the inter-model spreads.

In summary, we find the surface feedback decomposition can achieve similar level of radiation closure to the TOA analysis when using ERA5 kernels, affirming the validity of kernels for diagnosing the surface radiative feedback. However, the results qualitatively vary depending on which kernel dataset is used, indicating errors in the computation of some kernels.

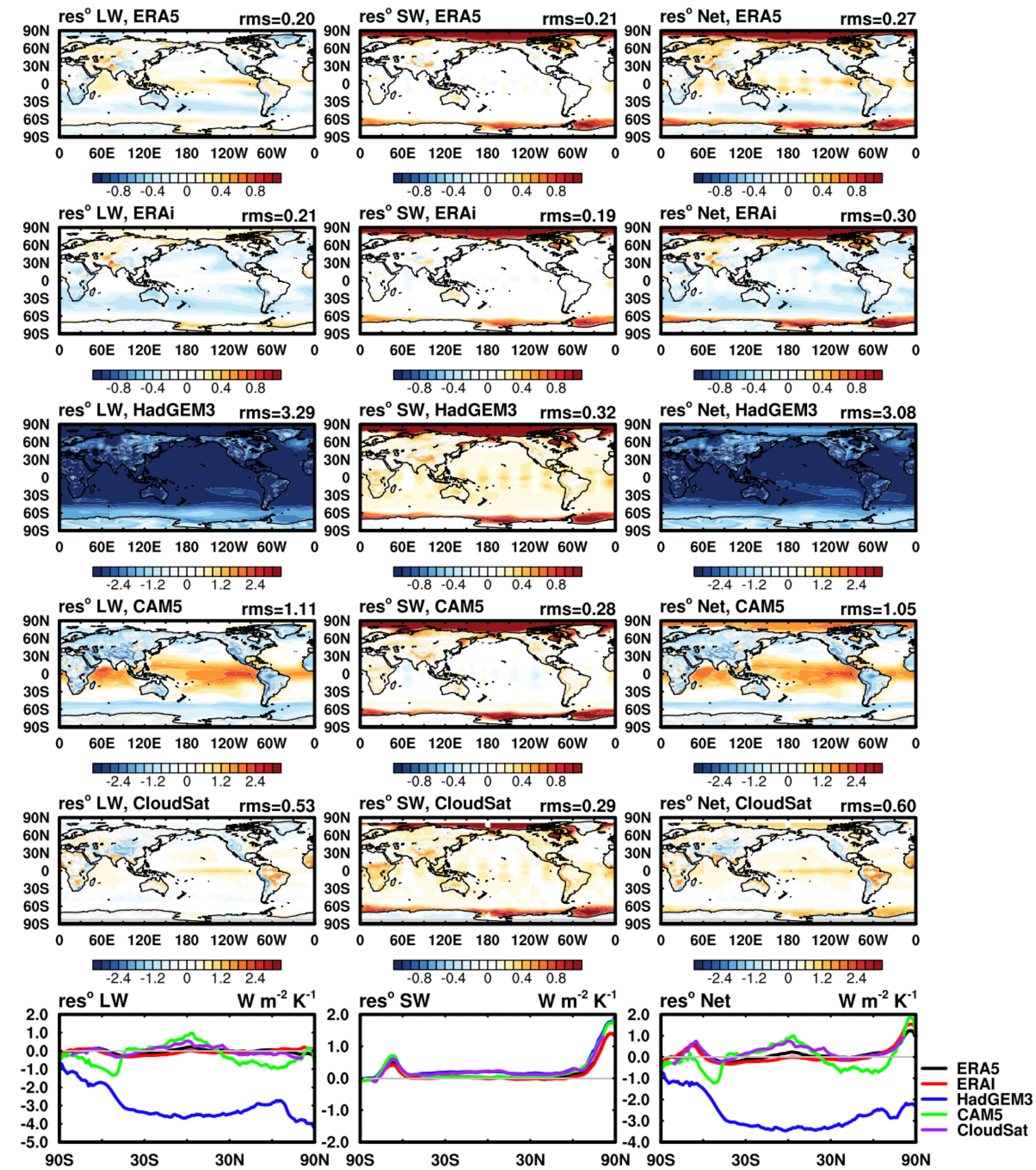


Figure 9. Similar to Figure 8, but for the surface feedback analysis.

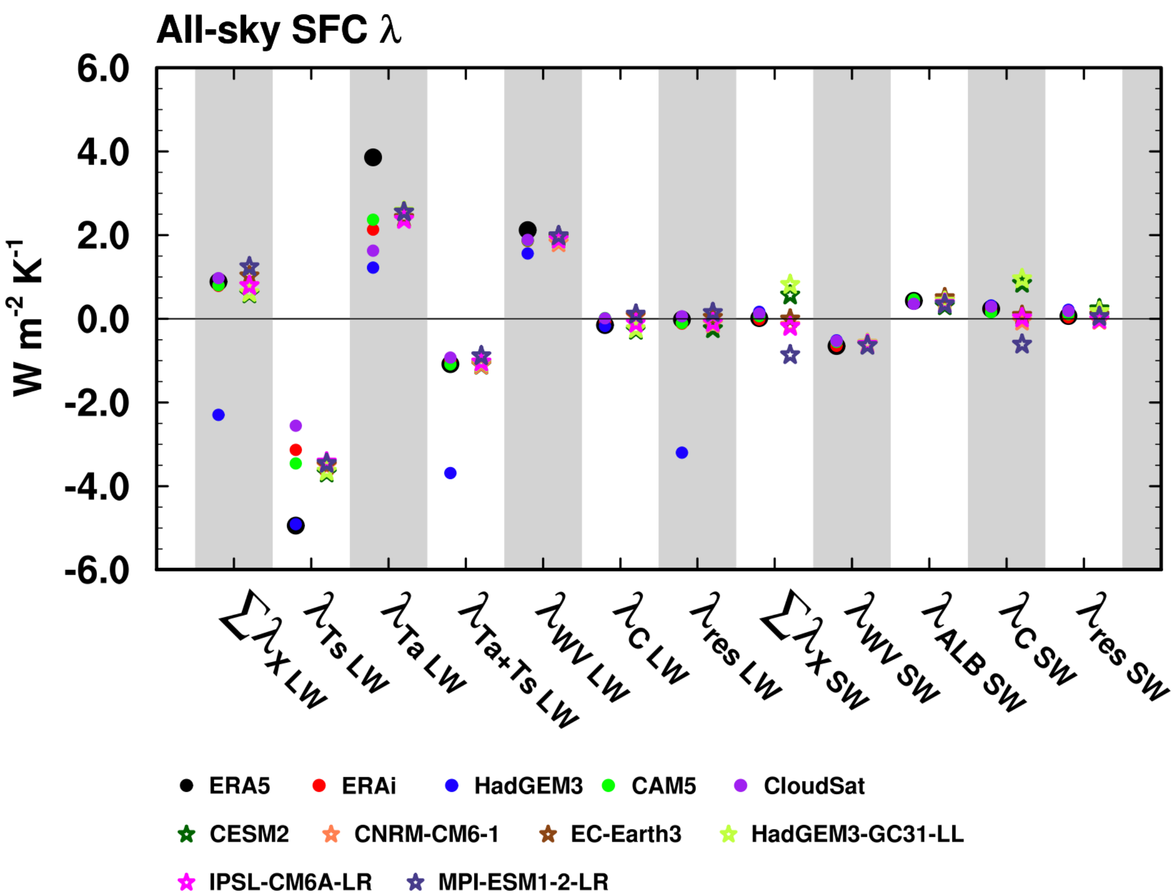


Figure 10. Similar to Figure 8, but for the surface feedback parameter.

## 5. Data availability

The datasets contain the multi-year averaged monthly mean TOA and surface kernel for surface temperature, air temperature, surface albedo and water vapor (LW and SW) and are available at: http://dx.doi.org/10.17632/vmg3s67568.2 (Huang and Huang, 2023).

## 6. Conclusions and discussions

In this paper, we present a newly generated set of ERA5-based radiative kernels of surface and air temperatures, water vapor and surface albedo, for both TOA and surface radiation fluxes. We also compare them with other published kernels, including the kernel values and the kernel-diagnosed radiative feedbacks for both the TOA and surface radiation budgets.

For the TOA kernels, the results here affirm general consistency among the different kernel datasets, and the discrepancies are generally within 10% in terms of vertically integrated or globally averaged radiative sensitivity, although some relatively larger regional biases are noticed, including those in the surface temperature kernel in the tropics (Figure 3a), those in the surface albedo kernel in the Arctic (Figure 3q) and those in the water vapor shortwave kernel in the Antarctica (Figure 3m), which is partly due to the dependence of radiative sensitivity on background climate states.

For the surface kernels, more prominent inter-kernel differences are found. For example, the differences in the water vapor shortwave kernel in the Antarctic (Figure 3o) and in the surface albedo kernel in the Arctic (Figure 3s) can reach 30%. Some kernels have considerably biased air temperature sensitivity values in the bottom atmospheric layers, which is likely due to improper treatment in the perturbation experiments used for kernel computation. The differences in both TOA and surface kernels discovered here affirm the importance of validating the radiative sensitivity as noted by Huang and Wang (2019) and Pincus et al. (2020).

The investigation of interannual variability in ERA5 kernels affirm the dependence of radiative sensitivity on atmospheric state and the further comparison between ERAi and ERA5 kernel (Figure 5) reveals the effects of clouds on the kernel values, which explains the discrepancies of multi-kernel datasets (Figure 3).

Applying the different kernels to quantifying the TOA and surface radiative feedbacks, we find that for TOA feedback quantification, the ERA5 kernels are as accurate as other kernel datasets, while for surface feedback, ERA5 and ERAi kernels show superior accuracy compared with other datasets. Considering the strengths of the ERA5 dataset in representing the atmospheric states, we recommend the use of ERA5 kernels.

In addition, we compare the feedback differences caused by using different kernels and also the inter-GCM spread of the feedback values (when measured by the same kernel). We find the kernel difference is not a major cause of the inter-GCM TOA feedback spread (Figure 7 and 8). This finding is consistent with the previous assessments (e.g., Soden et al., 2008; Jonko et al., 2012; Vial et al. 2013).

Radiation closure tests show that the unexplained residuals are generally within 10% for both TOA and surface analyses in terms of the global mean feedback, affirming the validity of the kernels for feedback quantification for both budgets. This suggests that the large non-closure residuals reported in some previous studies (e.g., Vargas Zeppetello, et al., 2019) are likely due to kernel inaccuracy rather than the limitation of the kernel method. However, there are more significant local non-closures, for example, in the shortwave in the Arctic region and around the Antarctic continent, which is contributed, but cannot be fully explained, by the kernel uncertainty. This points to the accuracy limit of the kernel (linear) method and calls for more advanced methods, such as the neural network method (Zhu et al., 2019), for local feedback analysis.

**Author contributions**

HH produced the ERA5 radiative kernel and provided calculations of the inter-kernel comparison and feedback analysis. Both HH and YH led the writing of the manuscript.

**Competing interests**

The authors declare that they have no conflict of interest.

**Acknowledgements**

We thank Mark Zelinka, Ryan Kramer and one anonymous reviewer for their helpful reviews. We acknowledge the grants from the Natural Sciences and Engineering Research Council of Canada (RGPIN-2019-04511) and the Fonds de Recherché Nature et Technologies of Quebec (2021-PR-283823) that supported this research. H. Huang thanks Yonggang Liu, Jun Yang and Qiang Wei for hosting her visit at Peking University and assisting her with computing resources.

## References

Block, K. and Mauritsen, T.: Forcing and feedback in the MPI‐ESM‐LR coupled model under abruptly quadrupled CO2, Journal of Advances in Modeling Earth Systems, 5, 676-691, 2013.

Boucher, O., Servonnat, J., Albright, A. L., Aumont, O., Balkanski, Y., Bastrikov, V., Bekki, S., Bonnet, R., Bony, S., and Bopp, L.: Presentation and evaluation of the IPSL‐CM6A‐LR climate model, Journal of Advances in Modeling Earth Systems, 12, e2019MS002010, 2020.

Bright, R. M. and O'Halloran, T. L.: Developing a monthly radiative kernel for surface albedo<? xmltex\break?> change from satellite climatologies of Earth's shortwave<? xmltex\break?> radiation budget: CACK v1. 0, Geoscientific Model Development, 12, 3975-3990, 2019.

Chao, L.-W. and Dessler, A. E.: An assessment of climate feedbacks in observations and climate models using different energy balance frameworks, Journal of Climate, 34, 9763-9773, 2021.

Collins, W., Ramaswamy, V., Schwarzkopf, M. D., Sun, Y., Portmann, R. W., Fu, Q., Casanova, S., Dufresne, J. L., Fillmore, D. W., and Forster, P.: Radiative forcing by well‐mixed greenhouse gases: Estimates from climate models in the Intergovernmental Panel on Climate Change (IPCC) Fourth Assessment Report (AR4), Journal of Geophysical Research: Atmospheres, 111, 2006.

Colman, R. and McAvaney, B.: A study of general circulation model climate feedbacks determined from perturbed sea surface temperature experiments, Journal of Geophysical Research: Atmospheres, 102, 19383-19402, 1997.

Danabasoglu, G., Lamarque, J. F., Bacmeister, J., Bailey, D., DuVivier, A., Edwards, J., Emmons, L., Fasullo, J., Garcia, R., and Gettelman, A.: The community earth system model version 2 (CESM2), Journal of Advances in Modeling Earth Systems, 12, e2019MS001916, 2020.

Dessler, A. E.: A determination of the cloud feedback from climate variations over the past decade, Science, 330, 1523-1527, 2010.

Doelling, D. R., Loeb, N. G., Keyes, D. F., Nordeen, M. L., Morstad, D., Nguyen, C., Wielicki, B. A., Young, D. F., and Sun, M.: Geostationary enhanced temporal interpolation for CERES flux products, Journal of Atmospheric and Oceanic Technology, 30, 1072-1090, 2013.

Dong, Y., Armour, K. C., Zelinka, M. D., Proistosescu, C., Battisti, D. S., Zhou, C., and Andrews, T.: Intermodel spread in the pattern effect and its contribution to climate sensitivity in CMIP5 and CMIP6 models, Journal of Climate, 33, 7755-7775, 2020.

Donohoe, A., Blanchard-Wrigglesworth, E., Schweiger, A., and Rasch, P. J.: The effect of atmospheric transmissivity on model and observational estimates of the sea ice albedo feedback, Journal of Climate, 33, 5743-5765, 2020.

Döscher, R., Acosta, M., Alessandri, A., Anthoni, P., Arsouze, T., Bergman, T., Bernardello, R., Boussetta, S., Caron, L.-P., and Carver, G.: The EC-Earth3 Earth system model for the Coupled Model Intercomparison Project 6, Geoscientific Model Development, 15, 2973-3020, 2022.

Eyring, V., Bony, S., Meehl, G. A., Senior, C. A., Stevens, B., Stouffer, R. J., and Taylor, K. E.:

Overview of the Coupled Model Intercomparison Project Phase 6 (CMIP6) experimental design and organization, Geoscientific Model Development, 9, 1937-1958, 2016.

Hersbach, H., Bell, B., Berrisford, P., Hirahara, S., Horányi, A., Muñoz - Sabater, J., Nicolas, J., Peubey, C., Radu, R., and Schepers, D.: The ERA5 global reanalysis, Quarterly Journal of the Royal Meteorological Society, 146, 1999-2049, 2020.

Huang, H. and Huang, Y.: Nonlinear coupling between longwave radiative climate feedbacks, Journal of Geophysical Research: Atmospheres, 126, e2020JD033995, 2021.

Huang, H. and Huang, Y.: "Data for ERA5 radiative kernels", Mendeley Data, V2, doi: 10.17632/vmg3s67568.2, 2023

Huang, H., Huang, Y., and Hu, Y.: Quantifying the energetic feedbacks in ENSO, Climate Dynamics, 56, 139-153, 2021a.

Huang, Y. and Wang, Y.: How does radiation code accuracy matter?, Journal of Geophysical Research: Atmospheres, 124, 10742-10752, 2019.

Huang, Y., Huang, H., and Shakirova, A.: The nonlinear radiative feedback effects in the Arctic warming, Frontiers in Earth Science, 651, 2021b.

Huang, Y., Ramaswamy, V., and Soden, B.: An investigation of the sensitivity of the clear - sky outgoing longwave radiation to atmospheric temperature and water vapor, Journal of Geophysical Research: Atmospheres, 112, 2007.

Huang, Y., Xia, Y., and Tan, X.: On the pattern of CO2 radiative forcing and poleward energy transport, Journal of Geophysical Research: Atmospheres, 122, 10,578-510,593, 2017.

Huang, Y., Chou, G., Xie, Y., and Soulard, N.: Radiative control of the interannual variability of Arctic sea ice, Geophysical Research Letters, 46, 9899-9908, 2019.

Jonko, A. K., Shell, K. M., Sanderson, B. M., and Danabasoglu, G.: Climate feedbacks in CCSM3 under changing CO 2 forcing. Part I: Adapting the linear radiative kernel technique to feedback calculations for a broad range of forcings, Journal of Climate, 25, 5260-5272, 2012.

Kolly, A. and Huang, Y.: The radiative feedback during the ENSO cycle: Observations versus models, Journal of Geophysical Research: Atmospheres, 123, 9097-9108, 2018.

Kramer, R. J., Soden, B. J., and Pendergrass, A. G.: Evaluating Climate Model Simulations of the Radiative Forcing and Radiative Response at Earth's Surface, Journal of Climate, 32, 4089-4102, 2019a.

Kramer, R. J., Matus, A. V., Soden, B. J., and L'Ecuyer, T. S.: Observation - based radiative kernels from CloudSat/CALIPSO, Journal of Geophysical Research: Atmospheres, 124, 5431-5444, 2019b.

Mauritsen, T., Bader, J., Becker, T., Behrens, J., Bittner, M., Brokopf, R., Brovkin, V., Claussen, M., Crueger, T., and Esch, M.: Developments in the MPI - M Earth System Model version 1.2 (MPI - ESM1. 2) and its response to increasing CO2, Journal of Advances in Modeling Earth Systems, 11, 998-1038, 2019.

Mlawer, E. J., Taubman, S. J., Brown, P. D., Iacono, M. J., and Clough, S. A.: Radiative transfer for inhomogeneous atmospheres: RRTM, a validated correlated - k model for the longwave, Journal of Geophysical Research: Atmospheres, 102, 16663-16682, 1997.

Myhre, G., Kramer, R., Smith, C., Hodnebrog, Ø., Forster, P., Soden, B., Samset, B., Stjern, C., Andrews, T., and Boucher, O.: Quantifying the importance of rapid adjustments for global precipitation changes, Geophysical Research Letters, 45, 11,399-311,405, 2018.

Pendergrass, A. G. and Hartmann, D. L.: The atmospheric energy constraint on global-mean precipitation change, Journal of climate, 27, 757-768, 2014.

Pendergrass, A. G., Conley, A., and Vitt, F. M.: Surface and top-of-atmosphere radiative feedback kernels for CESM-CAM5, Earth System Science Data, 10, 317-324, 2018.

Pincus, R., Buehler, S. A., Brath, M., Crevoisier, C., Jamil, O., Franklin Evans, K., Manners, J., Menzel, R. L., Mlawer, E. J., and Paynter, D.: Benchmark calculations of radiative forcing by greenhouse gases, Journal of Geophysical Research: Atmospheres, 125, e2020JD033483, 2020.

Previdi, M.: Radiative feedbacks on global precipitation, Environmental Research Letters, 5, 025211, 2010.

Riihelä, A., Bright, R. M., and Anttila, K.: Recent strengthening of snow and ice albedo feedback driven by Antarctic sea-ice loss, Nature Geoscience, 14, 832-836, 2021.

Shell, K. M., Kiehl, J. T., and Shields, C. A.: Using the radiative kernel technique to calculate climate feedbacks in NCAR's Community Atmospheric Model, Journal of Climate, 21, 2269-2282, 2008.

Smith, C. J., Kramer, R. J., and Sima, A.: The HadGEM3-GA7. 1 radiative kernel: the importance of a well-resolved stratosphere, Earth System Science Data, 12, 2157-2168, 2020.

Soden, B. J. and Held, I. M.: An assessment of climate feedbacks in coupled ocean–atmosphere models, Journal of climate, 19, 3354-3360, 2006.

Soden, B. J., Held, I. M., Colman, R., Shell, K. M., Kiehl, J. T., and Shields, C. A.: Quantifying climate feedbacks using radiative kernels, Journal of Climate, 21, 3504-3520, 2008.

Taylor, K. E., Stouffer, R. J., and Meehl, G. A.: An overview of CMIP5 and the experiment design, Bulletin of the American meteorological Society, 93, 485-498, 2012.

Thorsen, T. J., Kato, S., Loeb, N. G., and Rose, F. G.: Observation-based decomposition of radiative perturbations and radiative kernels, Journal of climate, 31, 10039-10058, 2018.

Vargas Zeppetello, L., Donohoe, A., and Battisti, D.: Does surface temperature respond to or determine downwelling longwave radiation?, Geophysical Research Letters, 46, 2781-2789, 2019.

Vial, J., Dufresne, J.-L., and Bony, S.: On the interpretation of inter-model spread in CMIP5 climate sensitivity estimates, Climate Dynamics, 41, 3339-3362, 2013.

Voldoire, A., Saint - Martin, D., Sénési, S., Decharme, B., Alias, A., Chevallier, M., Colin, J., Gu érémy, J. F., Michou, M., and Moine, M. P.: Evaluation of CMIP6 deck experiments with CNRM - CM6 - 1, Journal of Advances in Modeling Earth Systems, 11, 2177-2213, 2019.

Wetherald, R. and Manabe, S.: Cloud feedback processes in a general circulation model, Journal of the Atmospheric Sciences, 45, 1397-1416, 1988.

Williams, K., Copsey, D., Blockley, E., Bodas - Salcedo, A., Calvert, D., Comer, R., Davis, P., Graham, T., Hewitt, H., and Hill, R.: The Met Office global coupled model 3.0 and 3.1 (GC3. 0 and GC3. 1) configurations, Journal of Advances in Modeling Earth Systems, 10, 357-380, 2018.

Yue, Q., Kahn, B. H., Fetzer, E. J., Schreier, M., Wong, S., Chen, X., and Huang, X.: Observation-based longwave cloud radiative kernels derived from the A-Train, Journal of Climate, 29, 2023-2040, 2016.

Zelinka, M. D., Klein, S. A., and Hartmann, D. L.: Computing and partitioning cloud feedbacks using cloud property histograms. Part I: Cloud radiative kernels, Journal of Climate, 25, 3715-3735, 2012.

Zelinka, M. D., Myers, T. A., McCoy, D. T., Po - Chedley, S., Caldwell, P. M., Ceppi, P., Klein, S. A., and Taylor, K. E.: Causes of higher climate sensitivity in CMIP6 models, Geophysical Research Letters, 47, e2019GL085782, 2020.

Zhang, B., Kramer, R. J., and Soden, B. J.: Radiative feedbacks associated with the Madden–Julian

oscillation, Journal of Climate, 32, 7055-7065, 2019.
Zhang, M. and Huang, Y.: Radiative forcing of quadrupling CO 2, Journal of Climate, 27, 2496-2508, 2014.
Zhang, Y., Jin, Z., and Sikand, M.: The top‐of‐atmosphere, surface and atmospheric cloud radiative kernels based on ISCCP‐H datasets: method and evaluation, Journal of Geophysical Research: Atmospheres, 126, e2021JD035053, 2021.
Zhou, C., Liu, Y., and Wang, Q.: Calculating the climatology and anomalies of surface cloud radiative effect using cloud property histograms and cloud radiative kernels, Advances in Atmospheric Sciences, 39, 2124-2136, 2022.
Zhou, C., Zelinka, M. D., Dessler, A. E., and Yang, P.: An analysis of the short-term cloud feedback using MODIS data, Journal of Climate, 26, 4803-4815, 2013.

**Appendix**

The ERA5 kernels are computed following Eq. (1) and the approach outlined in Section 2.2.

1. Surface variable kernels

To execute the partial radiative perturbation computations, the perturbations are prescribed as the following: for the 2D feedback variables, the surface temperature is increased by 1 K and the albedo is increased by 0.01 at each location. Hence, the units of the two kernels, $K_{Ts}$ and $K_{ALB}$ are W m$^{-2}$ K$^{-1}$ and W m$^{-2}$ %$^{-1}$, respectively. When applying them to feedback quantification, their feedbacks are quantified as

$$\Delta R_{Ts} = K_{Ts} \cdot \Delta T_S \qquad \text{(A1)}$$

$$\Delta R_{Alb} = K_{ALB} \cdot \Delta Alb \qquad \text{(A2)}$$

where $\Delta T_S$ should be measured in the units of K and $\Delta Alb$ in absolute values, i.e., the multiply of 1%.

2. Water vapor kernel

For the 3D feedback variables, the perturbations are applied to each of the 37 pressure layers (from 1hPa to 1000hPa) and one layer at a time. For the water vapor kernel, a 10% incremental perturbation of the water vapor concentration is used. To adapt to the convention used in the majority of the existing kernels, we convert the units of the kernels to represent the radiative flux change corresponding to an increase of water vapor concentration that conserves the relative humidity of the layer under a 1-K increase in air temperature, i.e., converting the units from W/(m$^2$ $\Delta q_0^{+10\%}$ 100hPa) to W/(m$^2$ $\Delta q_0^{+1K}$ 100hPa):

$$K_q^{+10\%} = \frac{\Delta R_0}{\Delta q_0^{+10\%}} \qquad \text{(A3)}$$

$$K_q^{+1K} = \frac{\Delta R_0}{\Delta q_0^{+1K}} = K_q^{+10\%} \cdot \frac{\Delta q_0^{+10\%}}{\Delta q_0^{+1K}} = K_q^{+10\%} \cdot \frac{\Delta q_0^{+10\%}}{q_0} \cdot \frac{e_s(T_0)}{e_s(T_0+1K)-e_s(T_0)} \qquad \text{(A4)}$$

Where $q_0$ is the unperturbed water vapor concentration, in units of kg kg$^{-1}$. $\Delta q_0^{+10\%}$ is a 10% increment in water vapor concentration. $e_s(T)$ is the saturated water vapor pressure under temperature $T$, and can be measured by empirical formulas; hence, $\Delta q_0^{+1K}$ can be measured as $q_0[\frac{e_s(T_0+1K)}{e_s(T_0)} - 1]$. Accordingly, when the water vapor kernel is used for water vapor feedback quantification, the feedback is measured as:

$$\Delta R_q = K_q^{+1K} \cdot \Delta q^{+1K} = K_q^{+1K} \cdot \frac{\Delta q}{\Delta q_0^{+1K}} = K_q^{+1K} \cdot \frac{\Delta q}{q_0} \cdot \frac{e_s(T_0)}{e_s(T_0+1K)-e_s(T_0)} \qquad \text{(A5)}$$

where $\Delta q = q - q_0$ measures the change in water vapor concentration and is normalized by $\Delta q_0^{+1K}$ to give the factor that is multipliable with the $K_q^{+1K}$ kernel value. If using the Clapeyron-Clausius relation, the above expression can be further approximated as

$$\Delta R_q = K_q^{+1K} \cdot \frac{\Delta q}{q_0} \cdot \frac{e_s}{(de_s/dT)\cdot 1K} = K_q^{+1K} \cdot \frac{\Delta q}{q_0} \cdot \frac{R_v}{L_v} \cdot \frac{T_0^2}{1K} \qquad \text{(A6)}$$

where $R_v$ and $L_v$ are the gas constant and specific latent heat of water vapor, respectively. Note that when the kernels are used, $T_0$ and $q_0$ typically take their values from the base climate appropriate to the application, e.g., the unperturbed climate of a GCM experiment, not necessarily the dataset used for kernel computation.

3. Air temperature kernel

For the air temperature kernel, to be consistent with the "inhomogeneous path treatment" that accounts for the vertically non-uniform temperature distribution within each discrete atmospheric layer (Mlawer et al., 1997), perturbations are added not only to the layer-mean temperature but also the temperature at the exiting boundary of radiative fluxes of interest (i.e., the upper boundary of each layer for the TOA flux and the lower boundary for the surface flux), to appropriately represent the physical temperature perturbation in each layer.

A meaningful test to affirm the validity of the air temperature kernel is a vertical sum test, i.e., a linear additivity test to verify the vertical integration of the kernel values reproduce the flux change, either at TOA or surface, in response to a whole-column air temperature increase of 1K. Figure A1 shows that the ERA5 kernel well passes this test. However, as shown by Figure 9, some kernels (e.g., HadGEM3 kernel) show much weaker radiative response at surface, possibly due to improper treatment of the air temperature perturbation in the kernel computation, which may lead to an underestimated air temperature feedback and large biases in the surface feedback analysis.

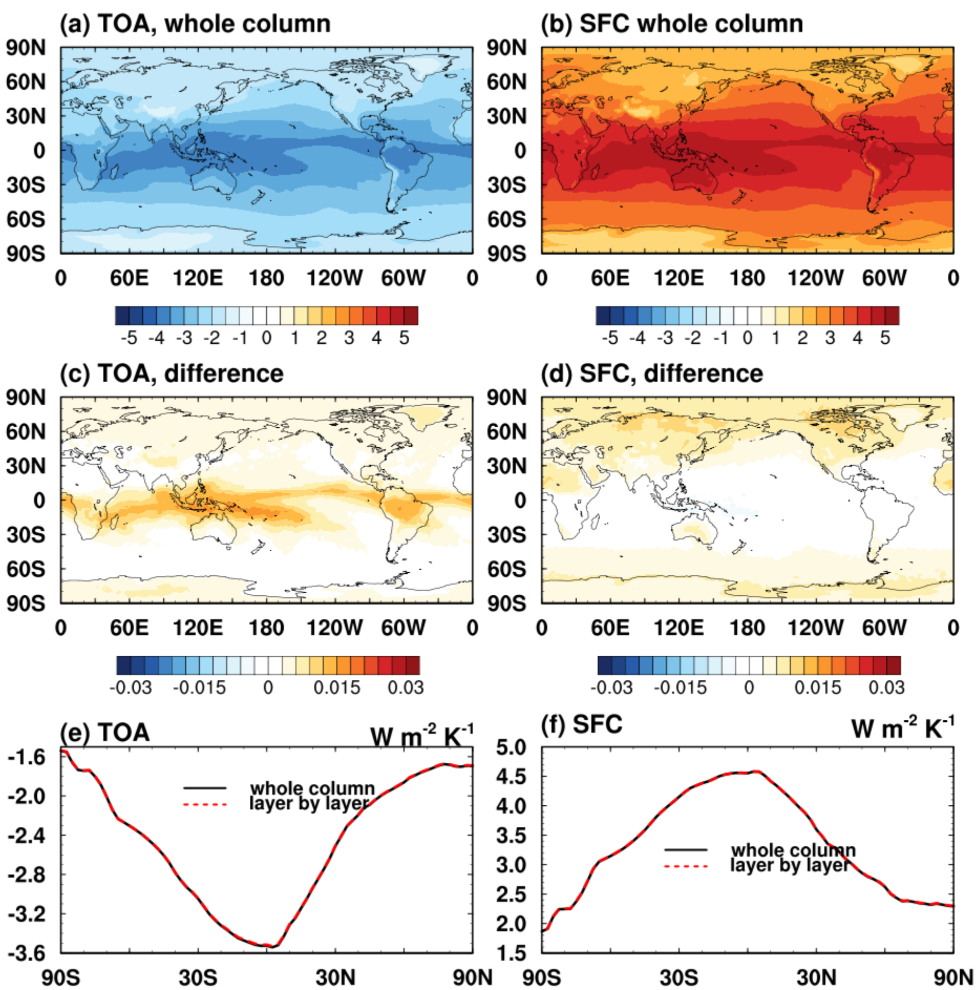

Figure A1. Monthly mean TOA and surface radiation flux change in response to a +1K air temperature perturbation throughout the vertical column: (a, b) computed by a radiation model, RRTMG; (c, d) difference of vertical sum of air temperature kernels compared to truth in (a, b); (e, f) comparison of the zonal mean.

Another challenge in the computation of air temperature kernel for surface flux is that the surface in radiative transfer models is also the lower boundary of the lowermost atmospheric layer. If the effects of the surface temperature perturbation on the emission of the surface and that of the lowermost atmospheric layer are not distinguished, this may lead to improper interpretation and use of the surface temperature kernel. In our ERA5 kernel, the two effects are considered separately: according to radiative transfer theory, an increase in surface skin temperature only affects the surface upward emission; an increase in air temperature only affects the downward radiation. In some other kernels such as CAM5, these effects are not distinguished, so that the kernel value represents the net effect, i.e., change in the sum of both downward and upward. As a result, in Table S4, we can only report the sum of surface and air temperature feedbacks. Figure A2 shows the comparison of vertically integrated air temperature kernels and the sum of surface and air temperature kernels between ERA5, CAM5, HadGEM3 and CloudSat. Although the strength of vertically integrated air temperature kernel for CAM5 is much weaker than that for ERA5 (Figure A2a and b), the sum of surface and air temperature kernel between these two datasets are in good agreement (Figure A2c and d), which warns that the seemingly right temperature feedback quantified by some kernels might come from the misattribution of surface temperature contributions. Another noticeable feature in Figure A2 is that the HadGEM3 kernel shows an underestimation in vertical integration of air temperature kernel and an overestimation in the sum of surface and air temperature kernel, likely due to mistreatment of the bottom layer, and this accounts for the biased surface feedback analysis as shown in Figure 9. Similar issues were noticed in Kramer et al. (2019a).

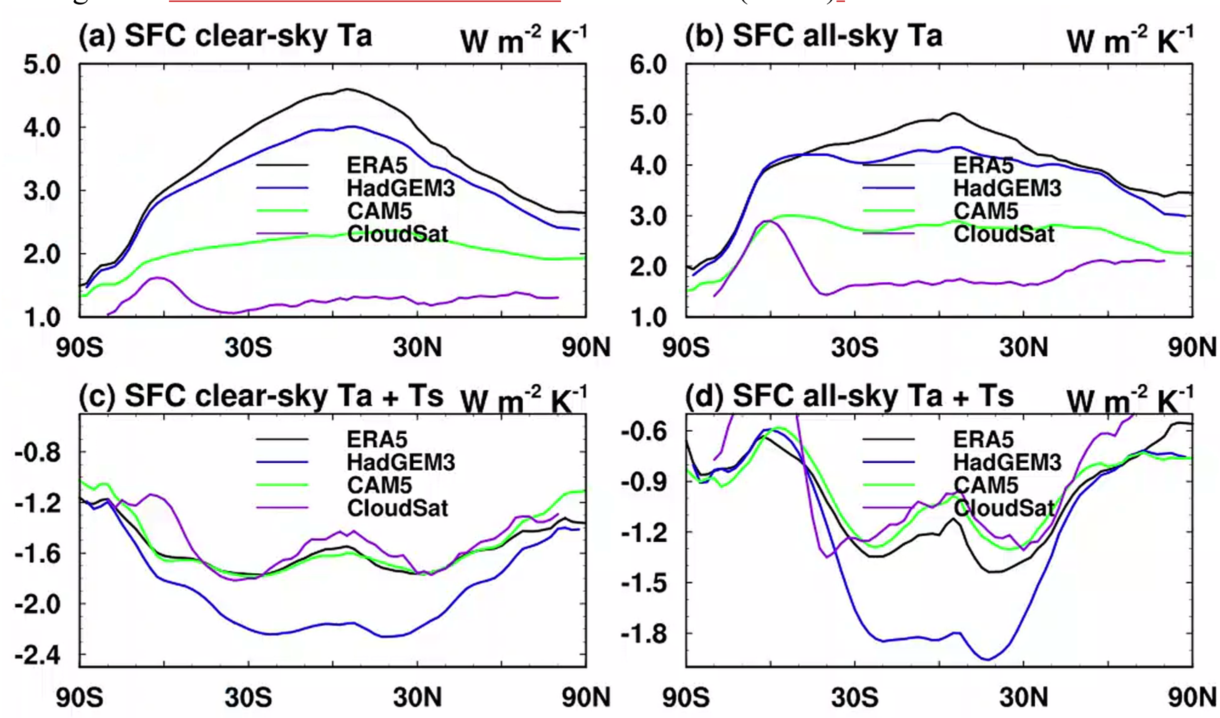

Figure A2. Comparison of annual mean surface kernels for ERA5, CAM5, CloudSat and HadGEM3 for (a, b) the vertically integrated air temperature kernel values, and (c, d) sum of surface and air temperature kernels.

4. Time averaging

As described in Section 2.2, all the kernels provided for feedback analysis are averaged from instantaneous kernel values over each calendar month and, in the ERA5 kernel, over multiple years. This is to ensure proper sampling of radiative sensitivity values under different atmospheric states, so that the kernels are representative of mean radiative sensitivity and thus can be readily multiplied with monthly mean climate responses ($\Delta X$) to evaluate climate feedbacks.

If the kernels are computed for fixed pressure levels, and if the pressure of any of these levels of an instantaneous atmospheric profile is higher than the surface pressure (i.e., the level is below the surface) at a time instance, this potentially creates inconsistency in the averaging procedure. To address this concern, we set the kernel value to zero (as opposed to missing value) before averaging. This is to ensure that when multiplied with the monthly mean climate response ($\Delta X$), the contribution of a pressure layer (e.g., that centered at 1000 hPa) is effectively counted only for the fraction of time the layer exists (when surface pressure is higher than 1000 hPa). Otherwise, the feedback quantification needs to be further weighted with fraction of time ($f$) when the pressure layer exists. For example, if the surface pressure is larger than 1000hPa only for half of time in a month ($f$=0.5), the radiation flux anomaly contributed by the layer centered at 1000 hPa is:

$$\Delta R_{T_{1000hPa}} = K^*_{T_{1000hPa}} \cdot \Delta T_{1000hPa} \cdot f \qquad \text{(A7)}$$

Here, $K^*_{T_{1000hPa}}$ represents the kernel value averaged from the time instances when the layer exists. Our averaging scheme is essentially to provide a kernel $K_{T_{1000hPa}} = K^*_{T_{1000hPa}} \cdot f$, so that it can be simply multiplied with $\Delta T_{1000hPa}$ to obtain the same result.

Figure A3 illustrates the differences between $K^*_{T_a}$ and $K_{T_a}$, in terms of their vertically integrated value. Such difference is pronounced over the Southern Oceans (around 60S), where the surface pressure value varies considerably. This likely explains why Figure 3h shows noticeable differences in the air temperature kernel in this region.

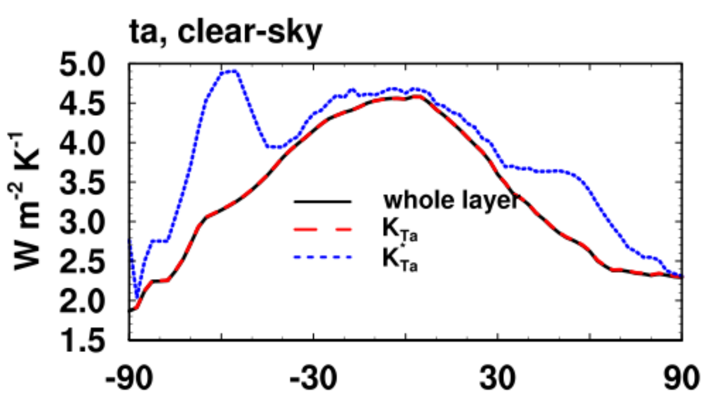

Figure A3. Zonal mean monthly mean air temperature kernels for surface flux from ERA5 in clear-sky. Black line is the result from the whole column perturbation computation by RRTMG, providing a "truth" for comparison. Red dashed line is the kernel weighted with fraction of time ($K_{T_a}$) and blue dotted line represents results without weights ($K_{T_a}^{*}$).

## 5. Layer-specified and layer thickness-normalized radiative kernels

We generate two versions of vertically resolved air temperature kernel, water vapor LW and SW kernel, one with values corresponding to specified vertical layers, i.e., in the units of W m$^{-2}$ K$^{-1}$, and another with unit-layer thickness (e.g., as shown in Figure 2 and 4), i.e., in W m$^{-2}$ K$^{-1}$ 100hPa$^{-1}$. The latter one properly portrays the vertical distribution of radiative sensitivity to perturbations in unit thickness layers, while the former one may be more convenient to use in feedback quantifications. For TOA budget analyses, these two versions of kernels lead to little difference in practice due to limited contributions from the bottom atmospheric layer. However, for surface budget analyses, we recommend using the layer-specified kernels, as the surface kernels typically show strongest sensitivity to the perturbations in the bottom layers, which can be best accounted for in the non-normalized kernels. Otherwise, the difference of surface pressure between ERA5 and GCMs needs to be carefully treated to avoid errors, for example, caused by missing the radiative contribution from the bottom layer of the atmosphere.